

UCLA

UCLA Electronic Theses and Dissertations

Title

Intrinsic Energy Dissipation Limits in Nano and Micromechanical Resonators

Permalink

<https://escholarship.org/uc/item/6g09t836>

Author

Iyer, Srikanth

Publication Date

2016

Peer reviewed|Thesis/dissertation

UNIVERSITY OF CALIFORNIA

Los Angeles

**Intrinsic Energy Dissipation Limits in Nano and
Micromechanical Resonators**

A dissertation submitted in partial satisfaction
of the requirements for the degree
Doctor of Philosophy in Electrical Engineering

by

Srikanth Subramanian Iyer

2016

© Copyright by
Srikanth Subramanian Iyer
2016

ABSTRACT OF THE DISSERTATION

Intrinsic Energy Dissipation Limits in Nano and Micromechanical Resonators

by

Srikanth Subramanian Iyer

Doctor of Philosophy in Electrical Engineering

University of California, Los Angeles, 2016

Professor Robert N. Candler, Chair

Resonant microelectromechanical Systems (MEMS) have enabled miniaturization of high-performance inertial sensors, radio-frequency filters, timing references and mass-based chemical sensors. Despite the increasing prevalence of MEMS resonators for these applications, the energy dissipation in these structures is not well-understood. Accurate prediction of the energy loss and the resulting quality factor (Q) has significant design implications because it is directly related to device performance metrics including sensitivity for resonant sensors, bandwidth for radio-frequency filters and phase-noise for timing references. In order to assess the future potential for MEMS resonators it is critically important to evaluate the energy dissipation limits, which will dictate the ultimate performance resonant MEMS devices can achieve. This work focuses on the derivation and evaluation of the intrinsic mechanical energy dissipation limit for single-crystal nano and micromechanical resonators due to anharmonic phonon-phonon scattering in the Akhiezer ($\Omega\tau \ll 1$) regime. The energy loss is derived using perturbation theory and the linearized Boltzmann transport equation for phonons, and includes the direction and polarization dependent mode-Grüneisen parameters in order to capture the strain-induced anharmonicity among phonon branches. Evaluation of the quality factor limit reveals that Akhiezer damping, previously thought to de-

pend only on material properties, has a strong dependence on crystal orientation and resonant mode shape. The robust model provides a dissipation limit for all resonant modes including shear-mode vibrations, which have significantly reduced energy loss because dissipative phonon-phonon scattering is restricted to volume-preserving phonon branches, indicating that Lamé or wine-glass mode resonators will have the highest upper limit on mechanical efficiency. Finally, the analytical dissipation model is integrated with commercial finite element software in order to evaluate the Akhiezer-limited Q for resonators with complex geometries and mode shapes and provide a prediction for the temperature dependence of the energy loss. This theory satisfies the pressing need for a reliable, analytical model that can predict the phonon dissipation limits for modern, resonant MEMS devices, where precise manufacturing techniques and accurate finite element methods can be used to select particular vibrational mode shapes and crystal orientations.

The dissertation of Srikanth Subramanian Iyer is approved.

Chandrashekhhar Joshi

Chee Wei Wong

Vidvuds Ozolins

Robert N. Candler, Committee Chair

University of California, Los Angeles

2016

TABLE OF CONTENTS

1	Introduction	1
2	Phonons in Crystalline Solids	12
2.1	Acoustic Phonon Dispersion	13
2.2	The Boltzmann Transport Equation for Phonons	16
3	Akhiezer Dissipation	18
3.1	Isotropic Akhiezer Loss	18
3.2	Anharmonic Akhiezer Dissipation	23
3.3	Perturbation Theory	24
3.4	Phonon BTE Solution	27
3.5	Energy Loss	30
3.6	Mode-Grüneisen Parameters and Third Order Elastic Moduli	33
3.7	Summary	35
4	Quality Factor	36
4.1	Mode- and Orientation-Dependent Energy Storage	36
4.2	Quality Factor	38
4.3	Analytical Results	40
5	Finite Element Modeling	45
6	Conclusion	60
	Appendix A Zener Model for Anelastic Relaxation in Solids	63

Appendix B Surface Dissipation	66
References	76

LIST OF FIGURES

1.1	Amplitude response of a resonator with a Lorentzian linewidth. The center frequency, f_0 is the resonant frequency and $\frac{f_0}{BW_{3dB}}$ is the quality factor (Q)	2
1.2	Operating principle for a MEMS vibratory rate gyroscope (adapted from Wang <i>et al.</i> [24]). Vibrations are driven along the x- and y- (drive) axes. (a) Under no rotation, there are four nodal points along the ± 45 deg (sense) axes. (b) Under a z-axis rotation, the Coriolis effect results in motion coupled from the drive mode to the sense mode. The sense mode displacement is proportional to the rotation rate and the quality factor.	4
1.3	Amplitude frequency response of low- Q resonators (solid line) with Q 's of 1,000 and high- Q resonators (dashed lines) with Q 's of 10,000. The high- Q resonators will function as narrowband filters, allowing for more precise binning of frequency signals.	5
1.4	An example of a massed-based chemical sensor, adapted from Hwang <i>et al.</i> [26]. The resonator schematics on the right show how nanoporous silicon etching was used to increase the surface area of the resonator so that more molecules can adsorb onto the surface, resulting in increased sensitivity of the chemical vapor. The sensitivity of mass-based chemical sensors is determined by the resonant frequency; however, the minimum detectible resolution is a function of the quality factor.	6
1.5	Level of understanding of various dissipation mechanisms in silicon resonators. The solid blocks represent known models, while the textured blocks represent the contributions of this work.	7

1.6	Comparison of the thermoelastic dissipation (TED) with the phonon-phonon dissipation (Akhiezer damping) and their relevance for different vibrational modes and resonant frequencies.	9
2.1	The simplest crystal is an infinite 1-D chain of identical atoms. The dispersion relationship can be solved using Newton's 2nd Law and the Bloch periodicity.	13
2.2	Phonon dispersion relationship for a 1-D chain of identical atoms (adapted from Kittel [37]). A minimum of zero occurs at $K = 0$ and a maximum of $(4C/M)^{1/2}$ occurs when $K = \frac{m\pi}{a}$, where m is an odd integer.	15
3.1	Description of Akhiezer dissipation for a single acoustic phonon branch. The plot on the left shows the phonon dispersion relationship at equilibrium (black) and under uniform tension (red). The plot on the right shows the equilibrium Bose-Einstein distribution (black). The perturbation of the phonon frequencies (and energies) due to the tensile strain results in an effective change in the slope of the dispersion relationship. As a result of this perturbation, the instantaneous phonon populations at all frequencies have non-equilibrium occupancy and they will relax towards their equilibrium concentrations via phonon-phonon scattering (blue arrow).	19

3.2 Anharmonic description of Akhiezer dissipation for a 1-D chain of atoms with three acoustic phonon branches. The plot on the left shows the phonon dispersion relationship at equilibrium (black) and under uniform tension (red). The plot on the right shows the equilibrium Bose-Einstein distribution (black) and the perturbed equilibrium distribution (dashed blue). The perturbation of the phonon frequencies (and energies) due to the strain may be different for each phonon branch and can even be opposite in sign. As a result of this anharmonicity among phonon modes, the instantaneous phonon populations will relax towards a perturbed Bose-Einstein distribution described by the average temperature among all phonon modes (dashed blue). 24

3.3 Wigner-Seitz cell for the diamond lattice centered about the Γ -point. (a) Three $\langle 100 \rangle$ directions (blue). (b) Six $\langle 110 \rangle$ directions (red). (c) Four $\langle 111 \rangle$ directions (green). There are 13 high-symmetry crystal directions and each contributes three pure modes, one longitudinal and two transverse, resulting in 39 distinct phonon branches. 25

3.4 Overview of the energy loss due to anharmonic phonon-phonon scattering. Strain in one of the normal directions ϵ_{1-3} leads to a perturbation of phonon frequencies in each branch, characterized by the mode-Grüneisen parameter $\gamma_{i,j}$, where j is the strain direction and i represents the crystal direction and polarization. For the diamond lattice, we can express i using the notation $[hkl]_P$, where $[hkl]$ is a particular crystal direction (expressed using Miller indices) and P is the polarization, which can be either longitudinal (L) or transverse (T_1 or T_2). The modulation of phonon frequencies (and energies) means the respective branch populations are out of equilibrium. Each branch distribution relaxes towards the perturbed equilibrium distribution via phonon-phonon scattering. The energy loss that occurs during this irreversible relaxation process is assumed to come from the acoustic wave, because that is the source of the perturbation. The shear strains ϵ_{4-6} , however, perturb fewer phonon branches due to the restriction that volume is preserved. 28

4.1 Woodruff’s isotropic expression compared with the rigorous anharmonic expression derived in this work. Our expression correctly incorporates mode- and orientation-dependent energy storage, parabolic frequency dependence due to the lag between the strain and the phonon distributions, and the anharmonic phonon perturbation, which is mode-dependent. Our anharmonic Q can be applied to all uniform modes given the strain vector $\vec{\epsilon}$ 39

4.2 Anharmonic and anisotropic $f \times Q$ product limits vs. mechanical resonant frequency at room temperature for WE, SE, CE and Lamé modes in [100] silicon. The solid lines represent the quality factor limits derived in this work (equation 4.3). The dashed line is Woodruff’s estimation of the Akhiezer damping limit and the points are experimental results from high quality factor resonators surveyed from the literature [54–67]. A number of recently fabricated resonators have quality factors that exceed Woodruff’s limit, indicating that the simplified, isotropic expression does not provide sufficient accuracy. 42

5.1 Finite element simulation (Comsol Multiphysics®) of higher-order modes of a $30\mu m$ wide, $150\mu m$ long and $5\mu m$ thick width extensional bulk acoustic resonator (WEBAR) from Pourkamali *et al.* [60]. (a) WEBAR mode with a simulated resonant frequency of 142MHz and measured frequency of 144MHz, (b) higher-order mode with simulated frequency of 419 MHz and measured frequency of 427 MHz, and (c) very complex higher-order mode with a simulated frequency of 664MHz and measured frequency of 764MHz. These modes are nearly impossible to solve for analytically, hence the need for finite element models in to predict both resonant frequency and energy dissipation limits. 46

5.2 The analytical Akhiezer dissipation calculation is applied to each individual mesh element. The energy loss and energy storage is then integrated over the volume of the structure in order to evaluate the quality factor. 47

5.3	High-level picture of the implementation of the Akhiezer dissipation calculation with commercially available finite element software. Matlab [®] is used to apply the material parameters (namely second-order elastic moduli) to the finite element model (FEM), the anisotropic mechanical mode shape is then simulated with the FEM software, and finally the results are extracted back to Matlab [®] in order to calculate energy storage and energy loss due to Akhiezer damping.	48
5.4	Simulated Akhiezer damping fQ versus experimentally measured fQ for several high- Q devices in the literature. The dashed green line is the fQ product limit due to Akhiezer damping and the solid black line is the measured fQ product. Within the solid block, the blue area is the fraction of the dissipation due to Akhiezer damping and the yellow area is the fraction due to other loss mechanisms. Q 's add inversely so an simulated Q that is twice the measured value indicates 50% of the loss is due to Akhiezer damping. (a)-(c) Three modes of the width-extensional bulk acoustic resonator (WEBAR) with a width of $30\mu m \times 150\mu m \times 5\mu m$ [60]. (d) A $400\mu m$ long concave bulk acoustic resonator (CBAR) where the center is narrower ($40\mu m$) than the end ($60\mu m$) [73]. (e) A length-extensional mode of a $600\mu m$ long, $20\mu m$ thick resonator, tethered at its center [74]. (f) $400\mu m \times 400\mu m \times 20\mu m$ Lamé mode resonator [74] (g) $1000\mu m \times 1000\mu m \times 46\mu m$ Lamé mode resonator [54]. . .	52
5.5	Mode-shape and simulated fQ product for a uniaxial extensional mode in single-crystal silicon as the device orientation is rotated counter-clockwise from the [100] direction towards the [110] direction. The simulation indicates an 17% increase in fQ for the [110] orientation compared to the [100] orientation.	54

5.6 fQ product versus temperature from 77K to 300K for a uniaxial extensional mode in anisotropic single-crystal silicon. Despite the appearance that the quality factor expression in equation 4.3 is inversely proportional to temperature, inclusion of the temperature dependence of all relevant material parameters, most notably the phonon lifetime τ reveals a positive temperature coefficient of Q (TCQ) with a value of 0.58. The inset of Figure 5.6 plots Q as a function of the phonon lifetime τ . As temperature is increased, the lifetime is reduced, so that the resonator operating conditions move from the blue circle towards the red circle. 56

5.7 fQ product versus temperature from 77K to 300K for a high-frequency (1GHz) extensional mode in anisotropic single-crystal silicon. The inset of Figure 5.6 plots Q as a function of the phonon lifetime τ . As temperature is increased, the lifetime is reduced, so that the resonator operating conditions move from the blue circle towards the red circle. Our Akhiezer damping model predicts a minimum at 120K, and a rapidly increasing Q as the temperature is cooled below this value. We note, however, that the Akhiezer damping model presented in this work assumes that $\Omega\tau \ll 1$, so that interpretation of the results when $\Omega\tau > 1$ is not reliable. . . . 57

5.8	Simulated Akhiezer-limited fQ product versus temperature from 77K to 300K for different modes and orientations of a single-crystal silicon square resonator. Again a weak (less than linear) increase in fQ with temperature is predicted. The results indicate that the same resonator operated in different modes may have up to 4x improvement in Akhiezer-limited Q . For applications where a specific mode-shape is not required, selecting different actuation electrodes and frequencies can potentially result in a higher quality factor.	59
B.1	Level of understanding of various dissipation mechanisms in silicon resonators. The main body of the text details a universal model for Akhiezer damping that provides a bulk limit on the quality factor of micromechanical due to phonon scattering, filling the gap in understanding. However, as devices are scaled to smaller sizes, bulk theories are no longer sufficient and new formulations that include the effects of finite sized resonators need to be developed.	67
B.2	A survey of published devices reveals a trend of decreasing Q with decreasing resonator size. This trend could be reversed with improved understanding of surface dissipation. Solid diamonds represent experiments performed at low temperature (<20 K), while hollow squares represent room temperature data.	68
B.3	Single-crystal silicon resonator showing (a) variations of device dimensions and (b) the torsional mode shape. Torsional modes are designed to be between 1 and 20 MHz.	69

B.4	Fabrication flow and scanning electron micrographs for sub-micron thick single-crystal silicon resonators. A series of thermal oxidation and HF etching steps are used to thin the device layer of a silicon-on-insulator wafer to a final thickness of less than 500 nm. A 400 nm thick thermal oxide remains and is used as a hard mask for the silicon etch that defines the resonator. Finally, the device is released via vapor HF etching to avoid stiction.	70
B.5	Schematic of the experimental setup used to measure the frequency response of single-crystal resonators. The resonator is mounted in the vacuum cryostat on top of a piezoelectric actuator that mechanical shakes the entire die. Motion is sensed via differential laser doppler vibrometry. A heater and temperature sensor along with continuous liquid nitrogen flow and a proportional-integral-derivative controller are used to vary the temperature between 77K and 400K.	71
B.6	Photograph of the experimental setup outlined in figure B.5. . . .	72
B.7	Quality factor as a function of temperature from 77K to 400K for [100] (solid blue) and [111] (solid red) oriented resonators fabricated in this work along with results from two other sub-micron thick single-crystal silicon resonators from the literature [76, 77]. All of these thin devices show a trend of increasing Q as a function of temperature around room temperature. The characteristic Debye minima may be indicative of a relaxation process. The resonant frequency variation (hollow blue circles) for the [100] oriented resonator follows the expected shift due to temperature dependence of the Young's modulus.	73

B.8 Quality factor for sub-micron thick single-crystal torsional resonators fabricated on [111] substrates with different monolayer coatings. These results (from [78]) show that the quality factor can vary up to five times by varying the monolayer coating. Interestingly, the ethyl, dodecyl and octadecyl coatings have roughly the same dissipation, suggesting that electronic surface structure plays a key role in the surface dissipation mechanism. 74

B.9 Fabrication flow for single crystal integrated P-I-N resonators on an silicon-on-insulator substrate. (a) Pattern and etch resonator layer from lightly doped p-type (yellow) silicon-on-insulator (SOI) wafer. (b) Pattern and implant P+ region (red) followed by N+ region (blue), ensuring surface doping via double implantation. (c) Pattern and etch metal contacts (gold). (d) HF vapor etch to undercut oxide and release. 75

B.10 2-D device simulation of a P-I-N integrated resonator depletion and accumulation under different biases using Taurus Medici. Carrier concentration can be controlled over nine orders of magnitude with reverse (-20V) and forward bias (+1.5V). The entire resonator (beams and paddle) is contained within the intrinsic region. . . . 75

LIST OF TABLES

4.1	Displacement profiles and elastic storage moduli for common vibration modes of a single-crystal rectangular parallelepiped with edges oriented along the $[100]$ directions.	37
-----	--	----

ACKNOWLEDGMENTS

My time at UCLA would not have been the same without tremendous support from my friends, family, and colleagues. First and foremost, I would like to thank my advisor, Prof. Rob Candler, who has always been and continues to be the most valuable resource I have on campus. I truly could not have asked for a more supportive and encouraging mentor for my graduate studies. I would also like to thank Prof. Vidvuds Ozolins for many invaluable theoretical discussions, as well as the remaining members of my dissertation committee, Prof. Chan Joshi and Prof. Chee Wei Wong, for their advice, encouragement and instruction.

It has been a pleasure working with the members of the Sensors & Technology Laboratory at UCLA. I would like to express my sincere gratitude to Yongha Hwang and Feng Gao for providing some of the infrastructure for resonator research in the lab, as well as Prof. Seungoh Han for his valuable simulation expertise and advice, Jack Cao for his assistance with semiconductor device simulations, and Ruben Acevedo for his help with resonator testing. I would also like to acknowledge Ghassan Malek and Brian Matthews for their fabrication support in the CNSI and NRF cleanroom facilities at UCLA. Lastly, thanks to Jere Harrison, Hyunmin Sohn, Omeed Paydar, Jimmy Wu, Sidhant Tiwari, Max Ho, Maggie Xiao, Ling Li and Yuan Dai for being great office mates.

Of course, I need to thank my friends who have always provided unwavering support and helped me live a balanced and fulfilling life outside of my graduate studies. Finally, I'd like to thank my mother, my father, my brother Shankar, and my sister Shailaja who continue to support and encourage all my endeavors.

VITA

- 2007 Graduated from Horace Greeley High School,
Chappaqua, NY.
- 2011 B.S. (Electrical Engineering), Minor (Mathematics),
Stanford University.
- 2012 Graduate Student Intern,
HRL Laboratories LLC, Malibu, CA.
- 2013 M.S. (Electrical Engineering),
University of California, Los Angeles.
- 2015 Teaching Assistant, Electrical Engineering Department,
EE 123B: Solid-State Physics II - Phonons and Magnetics
University of California, Los Angeles.
- 2011-present Graduate Student Researcher
Electrical Engineering Department
University of California, Los Angeles.

PUBLICATIONS

S. S. Iyer and R. N. Candler, “Mode- and direction-dependent mechanical energy dissipation in single-crystal resonators due to anharmonic phonon-phonon scattering”, Physical Review Applied 5, 034002 (March 4, 2016).

S. S. Iyer and R. N. Candler, “Mode- and Direction-Dependent Akhiezer Damp-

ing in *Single-Crystal Silicon Resonators*,” *Solid State Sensors, Actuators, and Microsystems Workshop (Hilton Head)*, 2016.

R. Perahia, J. J. Lake, S. S. Iyer, D. J. Kirby, H. D. Nguyen, D. T. Chang, “Electric gradient force drive mechanism for novel microscale all-dielectric gyroscope” *27th IEEE International Conference on MEMS*, January 2014.

S. S. Iyer, R. VEDAD-GHAVAMI, H. Lee, M. Liger, H. P. Kavehpour, and R. N. Candler, “Nonlinear damping for vibration isolation of microsystems using shear thickening fluid”, *Applied Physics Letters* 102, 251902 (2013).

S. Iyer, H. Lee, M. Liger, J. Judy, R. N. Candler, “Nonlinear Damping for Shock Protection of MEMS Devices Using Shear Thickening Fluid”, *Solid State Sensors, Actuators, and Microsystems Workshop (Hilton Head)*, 2012.

“Electric gradient force drive and sense mechanism for a micro-electro-mechanical-system gyroscope” with HRL Laboratories, LLC (filed June 28, 2013, issued January 1, 2015). US Patent No. 20150000401.

“Micro-resonator having lid integrated electrode” with HRL Laboratories, LLC (filed April 14, 2015). USPTO Application No. 14/686567.

CHAPTER 1

Introduction

For nearly three decades, miniaturized resonant devices have demonstrated unprecedented performance as inertial sensors, mass sensors, and frequency references and filters. Microelectromechanical (MEMS) resonators are currently used as the mechanical component for inertial sensors (accelerometers and gyroscopes) in automotive safety systems as impact sensors [1, 2], motion sensors for video game systems, gravity sensors for screen orientation in smartphones and have promising prospects for use in GPS-free navigation systems. Silicon and quartz resonators are now being integrated as timing references and frequency filters in cell phones, computers, and video games [3–11]. Resonators have also been investigated for use as highly sensitive chemical and biological sensors [12–17]. Additionally, resonators are key components in a number of measurement tools. Resonant cantilevers are employed in tapping mode scanning probe microscopy (STM and AFM) and as mass-based chemical sensors with zeptogram resolution [12, 18, 19]. Nanoscale resonators have also been used to investigate fundamental physical phenomena including detection of a single electron spin [20] and the quantum-mechanical ground state [21, 22].

A number of parameters may influence the performance of resonant MEMS devices including motional impedance, linearity, mode-matching, power handling and temperature drift; however, two key metrics, resonant frequency and the quality factor (Q), are of utmost importance for all resonator applications. The mechanical resonant frequency is the center frequency of the peak in the ampli-

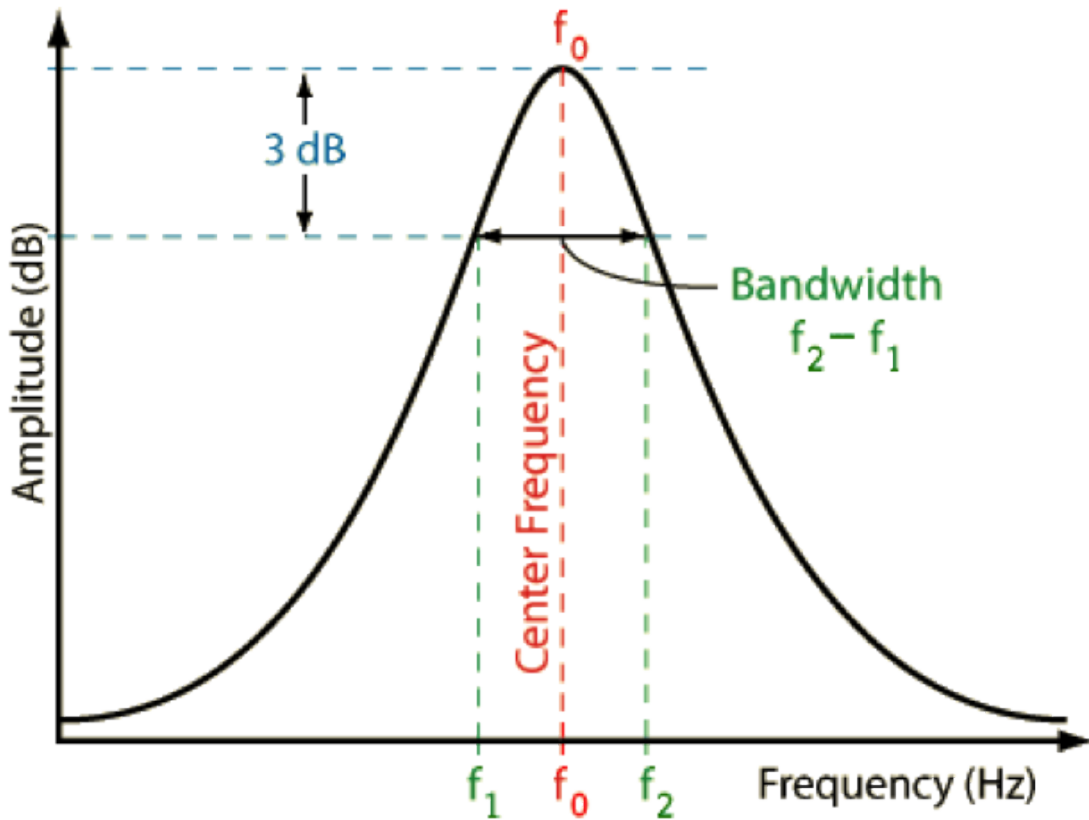


Figure 1.1: Amplitude response of a resonator with a Lorentzian linewidth. The center frequency, f_0 is the resonant frequency and $\frac{f_0}{BW_{3dB}}$ is the quality factor (Q)

tude response (Figure 1.1) of the structure and is well-understood and predicted using continuum mechanics and finite-element methods. The quality factor is experimentally determined as the resonant frequency divided by the 3dB bandwidth (assuming a Lorentzian lineshape). Physically, Q is 2π times the ratio of energy stored to energy lost per cycle of vibration (see equation 1.1). The energy storage is trivial to calculate and is equal to one half stress times strain for solids. Hence, the energy loss largely determines the quality factor. Q can be difficult to determine because a number of energy dissipation mechanisms may contribute to the loss. When the losses are small they add linearly, so the Q 's add inversely (equation 1.2). This implies that, often, a single dissipation mechanism will dominate the Q of the device, except when two loss mechanisms have the same order

of magnitude. Despite their wide range of uses, these resonator based systems all share a common limitation in that their performance is inherently limited by the amount of energy lost in the resonator.

$$Q = \frac{f_0}{BW_{3dB}} = 2\pi \frac{\text{Energy stored}}{\text{Energy loss per cycle}} \quad (1.1)$$

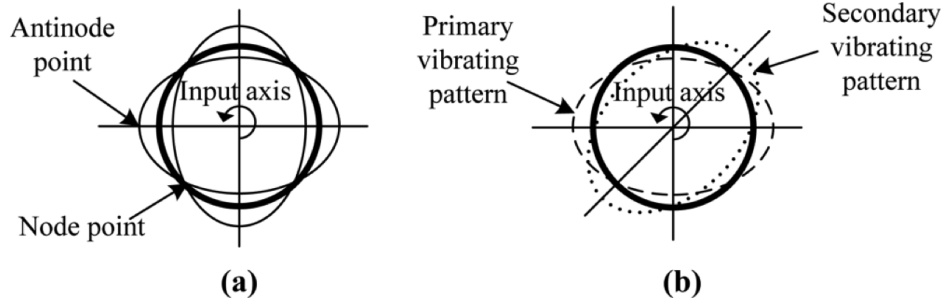
$$Q^{-1} = \sum \frac{1}{Q_i} = Q_{air}^{-1} + Q_{anchor}^{-1} + Q_{resistive}^{-1} + Q_{TED}^{-1} + Q_{ph-ph}^{-1} + Q_{surface}^{-1} + \dots \quad (1.2)$$

The dissipation can be difficult to determine because there is no single, predictive theory to evaluate the quality factor (Q), defined as $2\pi \frac{\text{Energy stored}}{\text{Energy loss per cycle}}$. Energy can be dissipated from the energy stored in the resonant vibrational mode to other acoustic modes or the environment [23]. A number of damping mechanisms, each requiring its own unique physical model, may contribute to the dissipation. Accurate prediction of Q has tremendous design implications because it is directly related to device performance metrics including sensitivity for resonant sensors, bandwidth for radio-frequency filters and phase-noise for timing references.

Figure 1.2 shows, schematically, the operating principle for a MEMS vibratory rate gyroscope (adapted from Wang *et al.* [24]). Figure 1.2(a) shows the standing wave pattern of a circular ring or disk resonator under no rotation. Vibrations are typically driven electrostatically by placing electrodes on the x- and y- (drive) axes. The mode shape for this actuation scheme results in four nodal points along the ± 45 deg (sense) axes for a symmetric, mode-matched resonator. Figure 1.2(b) shows the vibration under a z-axis rotation, where the Coriolis effect results in motion coupled from the drive mode to the sense mode. The displacement along the sense mode axes are given by equation 1.3, where y is the sense mode displacement, x_D is the drive mode displacement, Q is the quality factor of the resonator, Ω_z is the rotation rate about the z-axis and ω_0 is the resonant frequency of the ring or disk resonator. The displacement is, of course, proportional to the

rotation rate Ω_z as well as the quality factor Q . Hence, the sensitivity of the gyro will also be directly proportional to Q , so that increasing Q will lead to more sensitive rotation measurements.

$$|y| = \frac{2x_D Q}{\omega_0} \Omega_z \quad (1.3)$$



Rotation couples motion from the drive axis (0°) to the sense axis (45°) – Coriolis effect

Figure 1.2: Operating principle for a MEMS vibratory rate gyroscope (adapted from Wang *et al.* [24]). Vibrations are driven along the x- and y- (drive) axes. (a) Under no rotation, there are four nodal points along the ± 45 deg (sense) axes. (b) Under a z-axis rotation, the Coriolis effect results in motion coupled from the drive mode to the sense mode. The sense mode displacement is proportional to the rotation rate and the quality factor.

Radio-frequency (RF) applications for MEMS resonators include frequency filters and oscillators for timing. Both applications benefit from increased Q . For RF filters, Q is inversely related to bandwidth, as implied by equation 1.1. Figure 1.3 shows the amplitude frequency response of low- Q resonators (solid line) with Q 's of 1,000 and high- Q resonators (dashed lines) with Q 's of 10,000. Clearly the high- Q resonators will function as narrowband filters, allowing for more precise binning of frequency signals. For oscillators and frequency sources, high- Q leads to better frequency stability and reduced phase noise. Equation 1.4 gives the power spectrum ($L(\Delta\omega)$) of the phase noise assuming the Leeson model [25], where k

is Boltzmann’s constant, T is the temperature, P_s is the output power, ω_0 is the output frequency, $\Delta\omega$ is the frequency offset and Q is the quality factor. Here, we see that the phase noise is inversely proportional to the quality factor, implying that oscillators will benefit greatly from higher Q resonators.

$$L(\Delta\omega) = 10\log \left[\frac{2kT}{P_s} \cdot \left(\frac{\omega_0}{2Q\Delta\omega} \right)^2 \right] \quad (1.4)$$

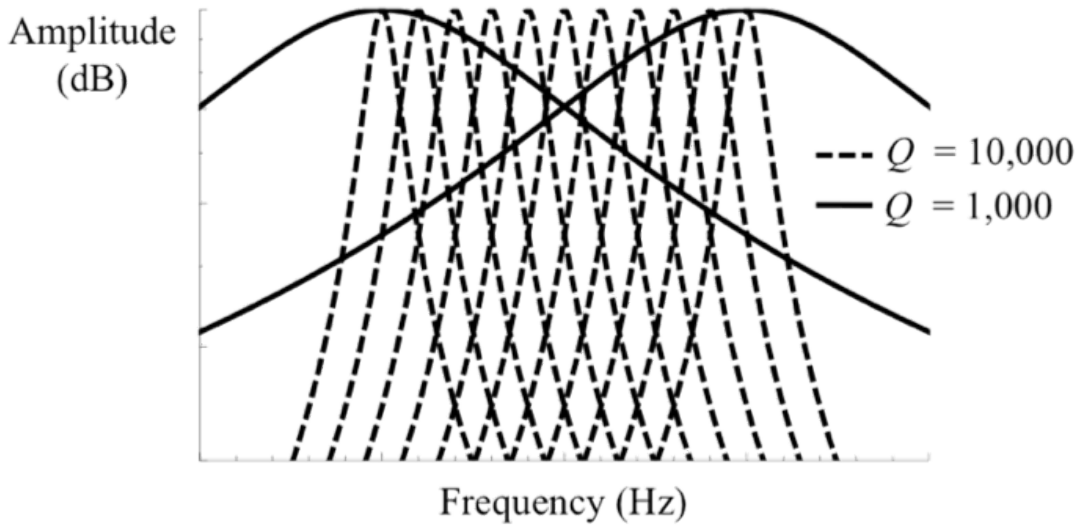


Figure 1.3: Amplitude frequency response of low- Q resonators (solid line) with Q 's of 1,000 and high- Q resonators (dashed lines) with Q 's of 10,000. The high- Q resonators will function as narrowband filters, allowing for more precise binning of frequency signals.

Resonators have also been employed as highly sensitive massed-based chemical sensors. When molecules are adsorbed on to the surface of the resonator, the mass will increase and the frequency will decrease. The sensitivity of the sensor is determined by the resonant frequency itself, which is related to the mass-stiffness ratio. Figure 1.4, adapted from Hwang *et al.* [26], shows an example of a massed-based chemical sensor, where the sensitivity was improved by increasing the porosity of the surface so that more molecules will adsorb onto the resonator resulting in

improved sensitivity. However, the resolution or minimum detectible mass is determined by Q . Higher Q 's allows for more sensitive determination of frequency shifts. Resonator based mass sensors have already achieved impressive zeptogram level resolutions, indicating the ability to detect single molecules or atoms [18].

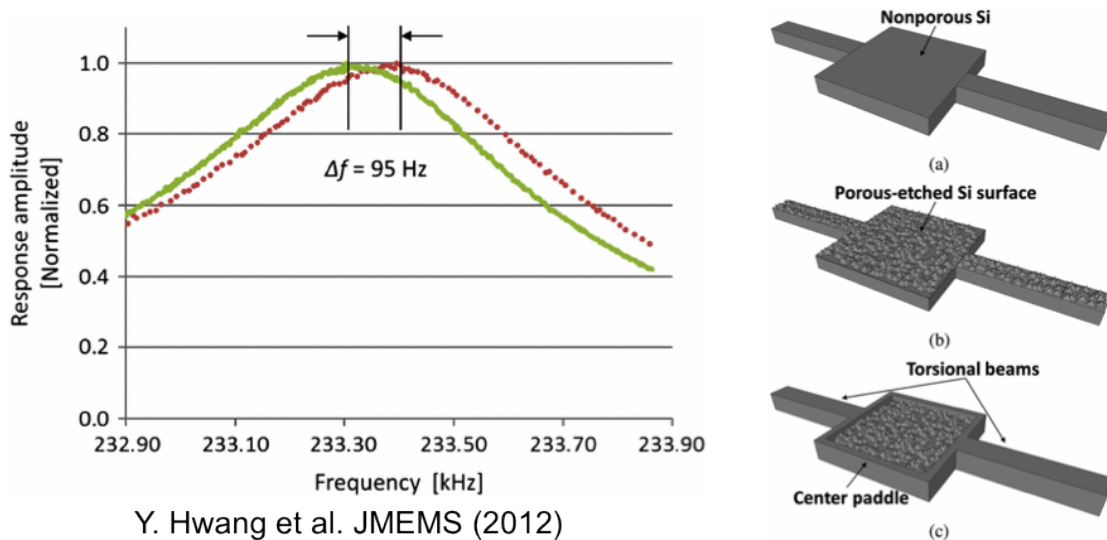
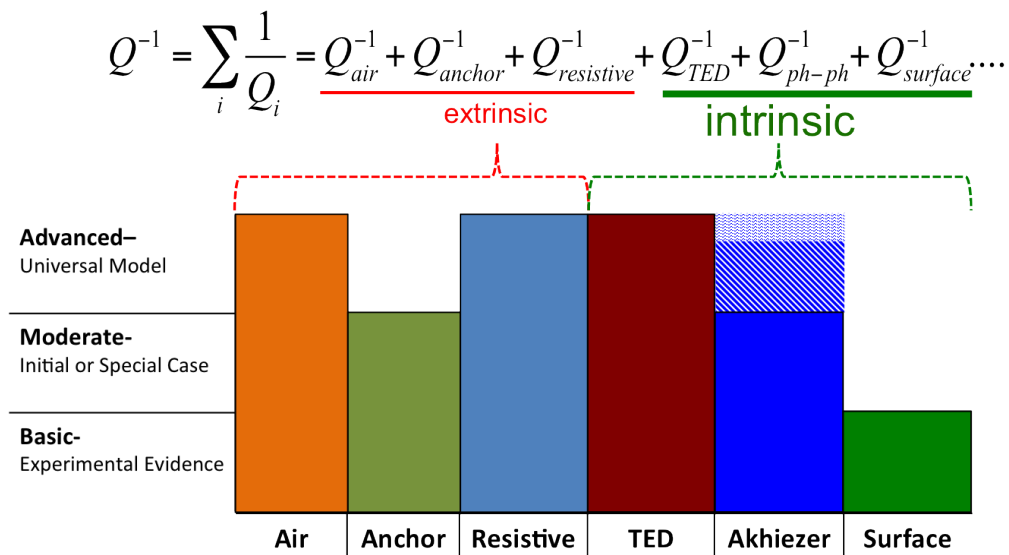


Figure 1.4: An example of a massed-based chemical sensor, adapted from Hwang *et al.* [26]. The resonator schematics on the right show how nanoporous silicon etching was used to increase the surface area of the resonator so that more molecules can adsorb onto the surface, resulting in increased sensitivity of the chemical vapor. The sensitivity of mass-based chemical sensors is determined by the resonant frequency; however, the minimum detectible resolution is a function of the quality factor.

The previous examples show that Q is directly related to a number of important performance metrics including, but not limited to, sensitivity. Figure 1.5 shows the level of understanding of various dissipation mechanisms in silicon resonators. Energy loss mechanisms may be intrinsic, fundamental to the material and device geometry, or extrinsic, a function of the operating environment of the resonator. Extrinsic damping mechanisms include air-damping due to ambient pressure, anchor loss due to acoustic energy leaking out of tethers to the sub-



8

Figure 1.5: Level of understanding of various dissipation mechanisms in silicon resonators. The solid blocks represent known models, while the textured blocks represent the contributions of this work.

strate or package and resistive losses to an external drive or sense circuit. This work, however, focuses on determining intrinsic dissipation limits in dielectric and semiconductor crystals, which are governed by the interaction between the elastic wave and thermal phonons. This interaction, also called internal friction, has two components: spatial phonon transport and local phonon scattering.

Time varying strain gradients drive irreversible spatial phonon transport (heat flow), known as thermoelastic dissipation (TED). In a flexural beam resonator, compression and tension on either side of the beam results in hot and cold regions, respectively, on either side of the beam. This thermal gradient across the width of the beam leads to irreversible heat flow from the hot area to the cold area. In 1937 Zener provided the first formalization of the thermoelastic loss [27, 28]. Briefly, his approach involved first solving the mechanical eigenmode ignoring thermal effects, using the this mechanical deformation to determine the result-

ing thermal gradients using the coupled heat equation, and finally inputting the thermal mode solution to the fully coupled mechanical equation to solve for the temperature-induced forces that are out of phase with the mechanical resonance. More recently, Duwel and Candler *et al.* solved the fully coupled mechanical and thermal equations simultaneously and solved for the TED numerically using a commercial finite element solver (Comsol Multiphysics[®]), allowing for determination of the TED for arbitrary geometries [29]. As a result, TED is now a well understood loss mechanism that can be accurately predicted using a finite element solver and can be minimized via appropriate design of device geometry [30, 31]. TED tends to be the dominant energy loss mechanism in flexural mode resonators due to the presence of tension and compression at any given point in time in the vibration cycle so that a large thermal gradient is present. For a perfectly uniform vibrational mode, the TED will be negligible due to the absence of strain-induced thermal gradients. Bulk mode vibrations are not perfectly uniform, but they do not have as steep a strain gradient as flexural modes do. At any given point during the vibration cycle for bulk modes, the entire solid is either under tension or compression, so that only a weak thermal gradient results. The TED is geometry dependent due to the dependence on the thermal diffusion time on the width of the beam, but we note that it becomes less significant as resonators approach the GHz regime due to a mismatch between the time constant for heat transfer and the mechanical vibration period. A simplified illustration of the thermoelastic loss along with Zener’s formulation for the resulting quality factor are given on the left side of Figure 1.6.

Thus, for high-frequency and bulk-mode resonators, the dissipation is ultimately limited by local phonon-phonon scattering, commonly referred to as Akhiezer damping. We note that Akhiezer damping is present in all vibrational modes, but tends to be observed in bulk modes, where the thermoelastic loss is significantly reduced. Thus, in many ways Akhiezer damping represents an lower

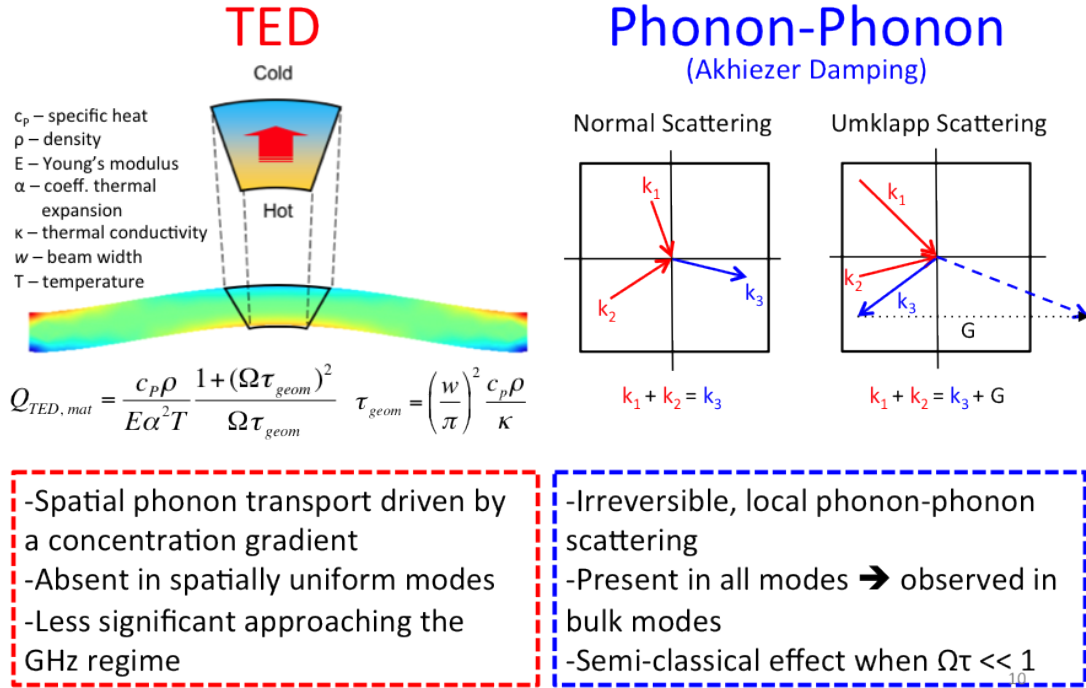


Figure 1.6: Comparison of the thermoelastic dissipation (TED) with the phonon-phonon dissipation (Akhiezer damping) and their relevance for different vibrational modes and resonant frequencies.

bound on the dissipation (and upper bound on Q) for mechanical resonators. The Akhiezer dissipation is determined semi-classically using the Boltzmann transport equation for phonons. The effect of the periodic strain in the resonator is to perturb the frequencies (and energies) of thermal phonons (also referred to as acoustic phonons). As a result these thermal phonons will have non-equilibrium populations and will attempt to relax back towards the equilibrium phonon distribution by redistributing amongst themselves via phonon-phonon scattering. In silicon resonators two types of phonon scattering are present: Normal processes and Umklapp processes. Both processes are three-phonon interactions where two acoustic phonons combine to form a third. In normal scattering, the momentum of the two input phonons is relatively small so that their combined momentum is

contained within the first Brillouin Zone and can be summed together to determine the momentum of the third phonon (i.e., momentum is strictly conserved within the first Brillouin Zone). In Umklapp scattering, the momentum of the input phonons is larger so that the combined momentum lies outside the first Brillouin Zone. In order to retain the reduced zone model, the resulting third phonon is flipped over (hence the German term Umklapp) and the remaining momentum is said to be imparted onto the crystal in the form of a reciprocal lattice vector. Umklapp processes alone will lead to relaxation to thermal equilibrium while Normal processes alone cannot bring a perturbed phonon distribution to the thermal equilibrium distribution [32]. A simplified picture of the phonon scattering processes along with a summary of the key differences between TED and Akhiezer damping are given in Figure 1.6. Akhiezer provided the first formulation for this energy loss due to phonon scattering in 1939 [33], and later in 1961 Woodruff and Ehrenreich provided a simplified evaluation assuming an isotropic material and assuming all acoustic phonon modes are perturbed identically. Woodruff's formulation allows for simple estimation of an order of magnitude result for a given material system; however, several modern devices have surpassed this isotropic limit, indicating the need for a more reliable analytical model that can describe the Akhiezer loss in MEMS devices. Other formulations have been introduced in the past [32, 34–36], but these formulations have not been readily adopted due to the complexity of evaluation or lack of analytical rigor. In this work, we derive a new expression for Akhiezer loss that captures the effect of anharmonic phonon-phonon scattering as well as crystalline anisotropy and vibrational mode shape. Additionally, we explain in detail the necessary assumptions required to enable simple evaluation of the resulting quality factor and integration of this model with commercial finite element software in order to provide a universal Akhiezer damping model that can be applied to arbitrary geometries with complex mode shapes. Finally, we use the finite element Akhiezer analysis to provide a reliable

Akhiezer limit and show that the energy loss in several of the highest Q silicon resonators in the literature is primarily due to the Akhiezer effect. Due to the fact that many applications of MEMS resonators are driven by high mechanical quality factor, it is critical to know if modern devices have reached the intrinsic limit, or if there is still room for improvement.

CHAPTER 2

Phonons in Crystalline Solids

Phonons are quantized modes of vibrations in a crystal lattice. The study of phonons is critical in solid-state physics, as phonon contributions largely determine many physical properties of insulating and semiconductor solids including elasticity, thermal properties such as the specific heat and thermal conductivity, and even electrical properties such as electrical conductivity and carrier mobility. Phonons are the elementary vibrations of a lattice and describe the normal vibrational modes, where each atom in the lattice vibrates at the same frequency. Ultimately, the classical mechanical result states that all vibrational modes can be expressed as superpositions of the normal modes at various frequencies. Classically, these normal vibrational modes are waves; quantum mechanically phonons assume particle like behavior, including the quantization of both energy and momentum. Phonons are bosons, which means they have zero spin and have no limit on the number that can occupy a particular state (energy and momentum), hence the term Bose-Einstein condensate. If we consider a single normal mode, the occupation number will be related to the amplitude of the wave, just as the photon number is related to the intensity of the electromagnetic wave.

At zero temperature (0 Kelvin), there is no energy in the system, so the crystal lattice is rigid and there are no phonons (i.e., the phonon occupation is zero). At non-zero temperature, the energy of the lattice is also non-zero and will have random fluctuations due to lattice vibrations (i.e., phonons), which we typically categorize as heat. At thermal equilibrium, the average number of phonons follows

the Bose-Einstein distribution

$$\langle n(\omega) \rangle = \frac{1}{\exp(\frac{\hbar\omega}{k_B T}) - 1} \quad (2.1)$$

where $\langle n(\omega) \rangle$ is the average phonon occupation at an angular frequency ω , k_B is Boltzmann's constant and T is the ambient temperature. The phonon energy is simply $\hbar\omega$.

2.1 Acoustic Phonon Dispersion

The simplest crystal lattice is a infinite, 1-D chain of identical atoms separated by a distance a (see Figure 2.1). Following the approach from Kittel, we can consider these atoms to be connected by linear springs with spring constant C , which describe interatomic force between neighboring atoms and assumes a symmetric, parabolic energy potential about the equilibrium interatomic spacing [37]. We assume that these interatomic 'springs' obey Hooke's law, where the force is



Figure 2.1: The simplest crystal is an infinite 1-D chain of identical atoms. The dispersion relationship can be solved using Newton's 2nd Law and the Bloch periodicity.

proportional to the displacement from the equilibrium point. The net force on the n^{th} atom is

$$F_{net} = C(u_{n+1} - u_n) + C(u_{n-1} - u_n) \quad (2.2)$$

The two terms on the right side of the above equation describe the force on the n th atom due to the neighboring atom on the right ($n - 1$) and left ($n + 1$) side, respectively. Using Newton's 2nd Law we can now describe the displacement u_n

of the n th atom in the lattice as

$$M \frac{d^2 u_n}{dt^2} = C(u_{n+1} + u_{n-1} - 2u_n) \quad (2.3)$$

where M is the mass of the atom. Now, we assume that the displacements are time-harmonic traveling waves

$$u_n = u_0 e^{inKa} e^{-i\omega t} \quad (2.4)$$

where K is the wavenumber and a is the equilibrium interatomic distance. The first exponential term ensures that the wave is periodic with the interatomic distance, which is required because we are solving for the normal vibrational modes. The second exponential is the time harmonic component of the wave and u_0 is the amplitude of the wave. Thus, the acceleration (second derivative of displacement) can be re-written as

$$\frac{d^2 u_n}{dt^2} = -\omega^2 u_n \quad (2.5)$$

and equation 2.3 can be expressed as

$$-\omega^2 M u_0 e^{inKa} = C u_0 \{e^{i(n+1)Ka} + e^{i(n-1)Ka} - 2e^{inKa}\} \quad (2.6)$$

Now, eliminating $u_0 e^{inKa}$ from all terms yields

$$\omega^2 M = -C[e^{iKa} + e^{-iKa} - 2] \quad (2.7)$$

Using the trigonometric identity $e^{iKa} + e^{-iKa} = 2\cos(Ka)$. The dispersion relationship can be written as

$$\omega^2 = (2C/M)[1 - \cos(Ka)] = (4C/M)\sin^2(Ka/2) \quad (2.8)$$

where the phonon frequency ω is a function of the wavenumber K . The dispersion is, equivalently the relationship between the phonon energy $H = \hbar\omega$ and the momentum $p = \hbar K$. The cosine in the expression for the dispersion indicates that a minimum frequency value occurs at the zone center $K = 0$ and a maximum

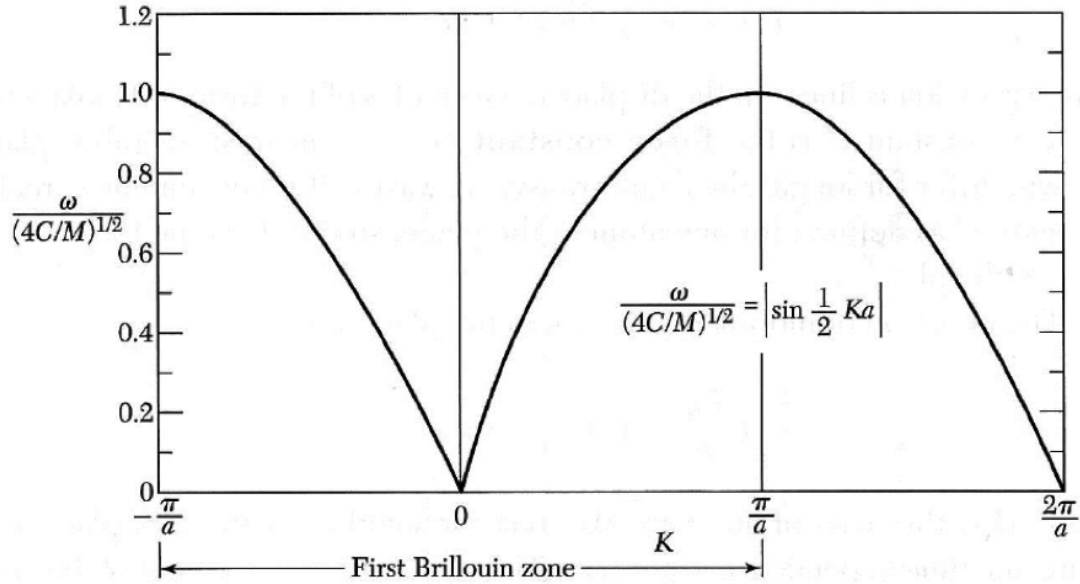


Figure 2.2: Phonon dispersion relationship for a 1-D chain of identical atoms (adapted from Kittel [37]). A minimum of zero occurs at $K = 0$ and a maximum of $(4C/M)^{1/2}$ occurs when $K = \frac{m\pi}{a}$, where m is an odd integer.

occurs when $K = \frac{m\pi}{a}$, where m is an odd integer. The dispersion is plotted below in Figure 2.2 (adapted from Kittel [37]). The dispersion is periodic with a period of $2\pi/a$. Thus, to fully describe the normal modes we need only consider the first Brillouin Zone (BZ), $-\pi/a < K < \pi/a$ for phonon calculations. Often, this sinusoidal dispersion relationship is approximated by a linear relationship $\omega = cK$, where c is the speed of sound in the medium.

The derivation of the dispersion relationship above assumes motion of atoms along the length of the chain; this is the longitudinal mode. However, the atoms can also vibrate along the remaining two axes; these are called transverse modes. Thus, for a 1-D chain of atoms, there are three normal modes, one longitudinal and two transverse. For the case of the 1-D chain, the two transverse modes are degenerate. Typically, the speed of sound is reduced in the transverse directions, so that the slope of the dispersion relationship $\omega(K)$ is not as steep. In more

complex crystals with multiple crystal axes with different interatomic spacings, we can consider the normal modes to be those along the high-symmetry directions, with each direction having three polarizations.

2.2 The Boltzmann Transport Equation for Phonons

The Boltzmann transport equation (BTE) describes the difference in the distribution function, $N(t, \vec{r}, \vec{v})$ between two adjacent volume elements after a time displacement dt . It can be derived from the Liouville theorem of classical mechanics, which states that the distribution must be conserved as we follow a volume element along a flowline. In the absence of collisions the distributions are equal

$$N(t + dt, \vec{r} + d\vec{r}, \vec{v} + d\vec{v}) = N(t, \vec{r}, \vec{v}) \quad (2.9)$$

where \vec{r} is the position vector and \vec{v} is the velocity vector in Cartesian coordinates. With collisions (i.e., scattering) we can write

$$N(t + dt, \vec{r} + d\vec{r}, \vec{v} + d\vec{v}) - N(t, \vec{r}, \vec{v}) = dt \left(\frac{\partial N}{\partial t} \right)_{scattering} \quad (2.10)$$

To first order,

$$dt \frac{\partial N}{\partial t} + d\vec{r} \cdot \nabla_{\vec{r}} N + d\vec{v} \cdot \nabla_{\vec{v}} N = dt \left(\frac{\partial N}{\partial t} \right)_{scattering} \quad (2.11)$$

moving dt to the left-hand side

$$\frac{\partial N}{\partial t} + \vec{v} \cdot \nabla_{\vec{r}} N + \vec{a} \cdot \nabla_{\vec{v}} N = \left(\frac{\partial N}{\partial t} \right)_{scattering} \quad (2.12)$$

where \vec{a} is acceleration. Finally, converting the gradient with respect to \vec{v} to a gradient with respect to the wavevector \vec{k} , where the momentum $\vec{p} = \hbar\vec{k}$, gives the traditional form for the BTE.

$$\frac{\partial N}{\partial t} + \vec{v} \cdot \nabla_{\vec{r}} N + \vec{a} \cdot \nabla_{\vec{v}} N = \left(\frac{\partial N}{\partial t} \right)_{scattering} \quad (2.13)$$

This classical form is not easily applied to phonon calculations, so we convert it using Hamilton's relations

$$\frac{d\vec{p}}{dt} = -\frac{\partial H}{\partial \vec{r}} \text{ and } \frac{d\vec{r}}{dt} = \frac{\partial H}{\partial \vec{p}} \quad (2.14)$$

giving the semi-classical BTE

$$\frac{\partial N}{\partial t} + \frac{1}{\hbar} \left(\sum_{j=1}^3 \frac{\partial N}{\partial r_j} \frac{\partial H}{\partial k_j} - \frac{\partial N}{\partial k_j} \frac{\partial H}{\partial r_j} \right) = \left(\frac{\partial N}{\partial t} \right)_{\text{scattering}} \quad (2.15)$$

The terms on the left-hand side that depend on r_j and k_j are the spatial terms that determine the thermoelastic dissipation, while the time dependent terms describe the local phonon transport that determines the Akhiezer dissipation.

CHAPTER 3

Akhiezer Dissipation

3.1 Isotropic Akhiezer Loss

In the Akhiezer damping model, the strain produced by the mechanical wave modulates the phonon frequencies and, consequently, the local equilibrium phonon distribution. The phonon populations cannot change instantaneously and will relax towards the modulated equilibrium distribution via phonon-phonon scattering when the thermal relaxation time (τ) is significantly less than the period of the mechanical wave. Due to the application of rapidly varying strain and a finite τ , the time-dependent phonon populations lag behind their (perturbed) equilibrium value. This relaxation towards equilibrium is an entropy producing process that consumes energy from the elastic wave. It is important to note that the Akhiezer damping model only applies when the scattering rate ($1/\tau$) is significantly larger than the frequency (Ω) of the mechanical vibration, $\Omega\tau \ll 1$, which is the case at room temperature for commonly used acoustic materials like silicon, germanium and quartz [38].

Figure 3.1 shows, qualitatively, how the perturbation of phonon frequencies (and energies) leads to a dissipative relaxation. Consider a wave-packet of phonons with wavenumber k_0 and frequency ω_0 at thermal equilibrium. The occupation of this mode will simply be n_0 , as determined by the Bose-Einstein distribution at thermal equilibrium. The perturbation theory describes the modulation of the phonon frequencies due to an applied strain. Figure 3.1 shows, as an exam-

ple, a reduction in phonon frequencies due to the application of uniform, tensile strain. The perturbed frequency is now $\omega_0 + \Delta\omega$; however, the occupancy of this mode, instantaneously, is still n_0 . Thus, the phonons with frequency $\omega_0 + \Delta\omega$ have nonequilibrium populations. This drives the relaxation back towards the equilibrium Bose-Einstein distribution, which can only occur due to some type of phonon scattering. In Akhiezer damping, this relaxation is presumed to occur via Umklapp phonon-phonon scattering (a three-phonon interaction).

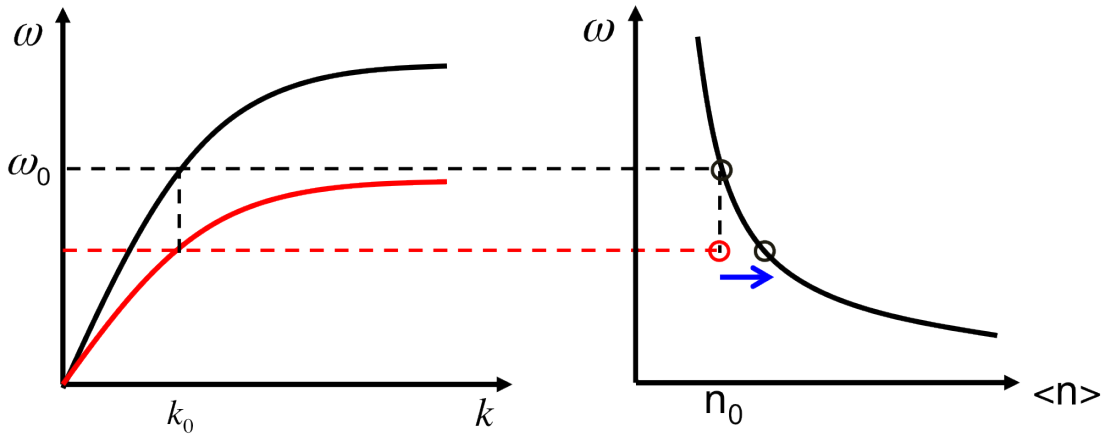


Figure 3.1: Description of Akhiezer dissipation for a single acoustic phonon branch. The plot on the left shows the phonon dispersion relationship at equilibrium (black) and under uniform tension (red). The plot on the right shows the equilibrium Bose-Einstein distribution (black). The perturbation of the phonon frequencies (and energies) due to the tensile strain results in an effective change in the slope of the dispersion relationship. As a result of this perturbation, the instantaneous phonon populations at all frequencies have non-equilibrium occupancy and they will relax towards their equilibrium concentrations via phonon-phonon scattering (blue arrow).

This limit on mechanical energy dissipation was first described by Akhiezer [33] and later solved by Woodruff using the linearized Boltzmann transport equation (BTE) and the Debye approximation to arrive at a simplified, isotropic expression

for internal friction (Q^{-1}) involving only classical, bulk parameters [39].

$$Q^{-1} = \frac{\gamma_0^2 C_v T}{\rho c^2} \Omega \tau \quad (3.1)$$

In the above expression, T is the ambient temperature, ρ is the material density, c is the Debye average sound velocity, C_v is the specific heat per unit volume and γ_0 is the average Grüneisen parameter associated with thermal expansion. Woodruff derived this result by assuming that all phonon modes are perturbed identically by the strain wave and neglecting the perturbation of the internal temperature of the solid. Typically, this expression is used to make an order of magnitude prediction of the internal friction limit in a given material [40]. While Woodruff's expression is conducive to simple evaluation of the Akhiezer damping limit, the assumption that all phonon modes are perturbed identically is flawed and obscures the fundamental physics behind the energy dissipation. As we will show rigorously in the next chapter, anharmonicity among phonon modes (i.e., the fact that all phonon modes are NOT perturbed identically) is actually what drives Akhiezer damping. Much like thermal expansion, we can trace the origin of the Akhiezer loss to the asymmetry of the interatomic potential that results from the fact that the attractive and repulsive forces between atoms scale differently with respect to the interatomic distance and is modeled by including third order elastic moduli.

Mason provides an alternate approach, arriving at an expression for internal friction by taking the derivative of the total phonon energy with respect to the applied strain and interpreting this as a loss modulus in accordance with Zener's phenomenological theory of anelastic relaxation in solids [34, 41]. Critically, Mason shows that because the dissipation originates from anharmonicity of phonon modes, third-order elastic coefficients can be used to estimate the mode-Grüneisen parameters, γ_i , which represent the strength of the phonon frequency perturbation to an applied strain for a particular pure phonon mode, i , characterized by a crystal direction and polarization. Thus, Mason dispenses with the assumption that

all phonon branches have the same γ_i in an attempt to provide a more accurate estimate of the Akhiezer damping limit.

Mason's derivation was heavily criticized by Barrett and Holland because of its lack of analytical rigor [42]; the most notable objections were the seemingly arbitrary designation of certain phonon frequency terms as strain-independent and the cursory assumption that the cutoff frequency in the Debye integral is strain-independent. Nevertheless, Mason's expression for acoustic attenuation appeared to provide better agreement with experimental results in silicon and germanium than Woodruff's simpler but more analytically sound expression. Consequently, Mason's (incorrect) expression is often cited when attempting to fit experimental data while Woodruff's is used to provide an upper bound on the quality factor (Q) for a given material system [40, 43]. A few refinements to Mason's method have been introduced including a correction factor for the Debye integral to account for the modulation of the upper integration limit [44] and Brugger-Fritz integration schemes to include phonon scattering to arbitrary directions [45]. Even with these corrections, Mason's expression is inherently flawed [46], so it should not be used to predict experimental results. Similarly, in an attempt to better match acoustic attenuation measurements, Nava *et al.* modified Woodruff's method by introducing a pure-mode ultrasonic Grüneisen parameter. They rigorously define this parameter as a weighted average of mode-specific phonon thermal conductivities, but cannot evaluate their complex expression and instead simply fit its value to experimental results [35]. Ultimately all these refinements require careful integration over the spectrum of acoustic phonon modes, which unnecessarily complicates evaluation of the energy dissipation.

More recently, Kiselev and Iafrate considered the internal friction for the specific case of a doubly-clamped, flexural mode cantilever and, following the approach introduced by Bommel and Dransfeld, showed qualitatively that the anharmonicity induced by the presence of just two groups of phonons with different

mode-Grüneisen parameters results in local phonon-phonon dissipation [36, 47]. However, they oversimplify their evaluation of the dissipation limit by assuming only two phonon groups and arbitrarily designating values for the mode-Grüneisen parameters for each group, prohibiting valid comparison with experimental data. Kunal and Aluru used molecular dynamics to calculate the Akhiezer limit for nickel nanowires with a maximum size of 20 atoms per edge [48]. Ultimately, likely due to the resonator size restriction imposed by the practical computational limitations, they do not compare the molecular dynamics results to experimental data, and only attempt to correlate their results to existing theory by evaluating Mason’s nonlinearity parameter, D , which we have already indicated is not an analytically sound choice. Hence, there is a compelling need for a more predictive, analytical model that employs appropriate simplifications so that the energy loss can be evaluated in a straightforward and consistent manner using known material constants and reliably compared with experimental results.

In this work, we rigorously derive an expression for the internal friction limit due to anharmonic phonon-phonon scattering that incorporates important elements of both Woodruff’s and Mason’s derivations. We solve for the energy loss using the analytically sound Boltzmann transport method, but rather than assuming all phonon modes are perturbed equally by strain, we include the directional and polarization dependent mode-Grüneisen parameters. The resulting expression for Akhiezer damping still depends only on bulk parameters, but distinguishes between different vibration modes and crystal directions. As we will show, for common vibration modes this expression can be reduced to match equation 3.1, but replacing the average Grüneisen parameter, γ_0 , with an anharmonic Grüneisen parameter, Γ_a , that depends on the strain profile of the vibration.

3.2 Anharmonic Akhiezer Dissipation

In order to accurately describe the physics behind the Akhiezer dissipation, we must adopt a more sophisticated interpretation that involves more than one phonon branch. In fact, as noted earlier, even a 1-D chain of identical atoms will have three acoustic phonon branches (one longitudinal and two transverse). We see in Figure 3.2 that the different phonon branches can be perturbed by different amounts. Strain may cause phonons in the L branch to be reduced in frequency, while those in the T_1 branch experience an increase. Similarly, phonons in the T_2 branch are shown to be reduced in frequency, but by a different amount than the L phonons. Thus, instead of considering equal perturbation among all modes described by the average Grüneisen parameter γ_0 , we must include the mode-Grüneisen parameters γ_i , which can be different for each phonon branch. The fact that the strength of the perturbation for each phonon branch is different will henceforth be described using the term anharmonicity. We can interpret this anharmonicity, qualitatively, as strain induced ‘heating’ and ‘cooling’ of individual phonon branches, where ‘hot’ branches are increased in energy and ‘cold’ branches are decreased in energy. Consequently, these hot and cold phonon branches will try to reach quasi-equilibrium amongst themselves. Rather than relaxing toward the equilibrium Bose-Einstein distribution (solid black), they will instead relax towards a modulated Bose-Einstein distribution described by a perturbed temperature $T + \Delta T$, where ΔT is determined as the average perturbation over all phonon modes. The irreversible relaxation still occurs via dissipative phonon-phonon scattering. Following this interpretation, a more descriptive term for Akhiezer damping is anharmonic phonon dissipation. We use both terms interchangeably in the remainder of this document.

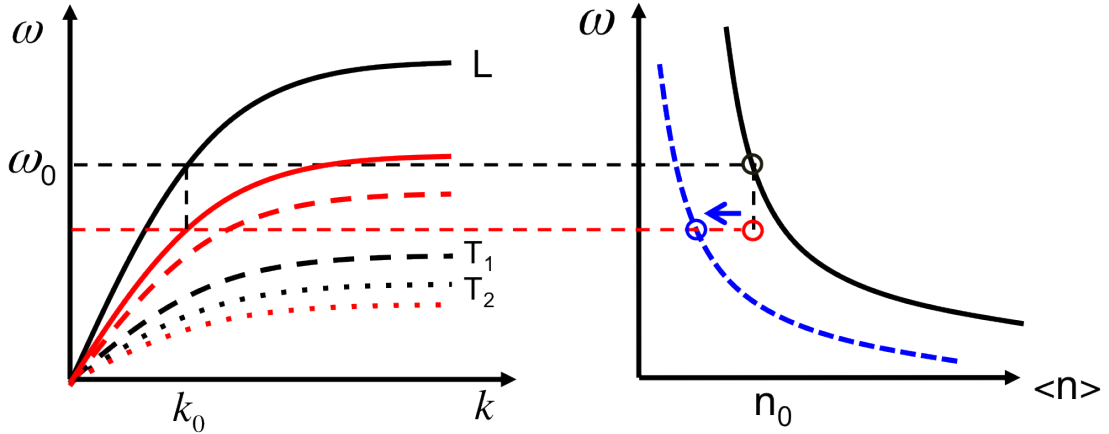


Figure 3.2: Anharmonic description of Akhiezer dissipation for a 1-D chain of atoms with three acoustic phonon branches. The plot on the left shows the phonon dispersion relationship at equilibrium (black) and under uniform tension (red). The plot on the right shows the equilibrium Bose-Einstein distribution (black) and the perturbed equilibrium distribution (dashed blue). The perturbation of the phonon frequencies (and energies) due to the strain may be different for each phonon branch and can even be opposite in sign. As a result of this anharmonicity among phonon modes, the instantaneous phonon populations will relax towards a perturbed Bose-Einstein distribution described by the average temperature among all phonon modes (dashed blue).

3.3 Perturbation Theory

Akhiezer damping describes the microscopic relaxation of acoustic thermal phonons due to a macroscopic strain wave. The loss is formulated using perturbation theory and the Boltzmann transport equation for phonons. The derivation of the anharmonic phonon-phonon dissipation begins with the assumption that the strain wave is time-harmonic with wavevector \mathbf{K} and angular frequency Ω so that $\epsilon(t) \propto \exp(i(\mathbf{K} \cdot \mathbf{r} - \Omega t))$, where \mathbf{r} is the position vector. The strain perturbs the

frequencies (ω) of all thermal phonons, satisfying the relation,

$$\omega_i = \omega_{i0}[1 + \vec{\gamma}_i \cdot \vec{\epsilon}(t)] = \omega_{i0} + \Delta\omega_i \quad (3.2)$$

where the index i denotes a pure-mode branch characterized by a direction and polarization along a crystal axis so that ω_i is the instantaneous phonon frequency of the i^{th} branch and ω_{i0} is the unperturbed equilibrium phonon frequency. Each high-symmetry direction in the Wigner-Seitz cell, the primitive Brillouin zone (BZ), has a longitudinal mode that is polarized along the direction of phonon propagation and two transverse modes that are polarized perpendicularly to the propagation direction. Figure 3.3 shows the 13 principal crystallographic directions (high-symmetry directions) in the Wigner-Seitz cell for the diamond lattice with the $\langle 100 \rangle$, $\langle 110 \rangle$ and $\langle 111 \rangle$ families of directions in distinct subplots. Deformation of the solid due to strain, even in just a single direction, deforms the entire BZ resulting in perturbation of all phonon branches.

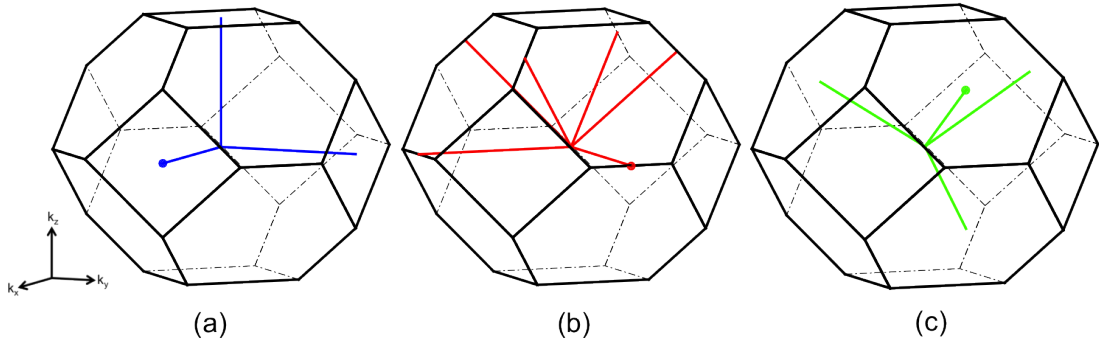


Figure 3.3: Wigner-Seitz cell for the diamond lattice centered about the Γ -point. (a) Three $\langle 100 \rangle$ directions (blue). (b) Six $\langle 110 \rangle$ directions (red). (c) Four $\langle 111 \rangle$ directions (green). There are 13 high-symmetry crystal directions and each contributes three pure modes, one longitudinal and two transverse, resulting in 39 distinct phonon branches.

For cubic crystals, the strain tensor is assumed to be symmetric, so we can express it compactly as a vector, $\vec{\epsilon}(t)$, with six independent components, denoted

ϵ_j , where the index j indicates one of the six possible strain directions: three normal and three shear (see equation 3.3).

$$\begin{bmatrix} \epsilon_{xx} \\ \epsilon_{yy} \\ \epsilon_{zz} \\ \epsilon_{yz} \\ \epsilon_{zx} \\ \epsilon_{xy} \end{bmatrix} = \begin{bmatrix} \epsilon_1 \\ \epsilon_2 \\ \epsilon_3 \\ \epsilon_4 \\ \epsilon_5 \\ \epsilon_6 \end{bmatrix} \quad (3.3)$$

Consequently, $\vec{\gamma}_i$ is also a vector with six components that are the mode-Grüneisen parameters, $\gamma_{i,j}$, corresponding to the anharmonic perturbation of the i^{th} branch frequency due to strain in the j^{th} direction. Here, we assume that the $\gamma_{i,j}$'s are independent of the phonon frequency and wavenumber. As a result, the instantaneous phonon population in each branch, N_i , deviates from its thermal equilibrium Bose-Einstein distribution, $N_{i0} = (e^{\hbar\omega_{i0}/k_B T} - 1)^{-1}$, so that

$$N_i = N_{i0} + \Delta n_i \quad (3.4)$$

Now, we use the linearized Boltzmann transport equation (BTE) to solve for N_i . We are deriving the dissipation limit due to local phonon-phonon scattering, so we assume uniform strain and can eliminate all spatial terms in the BTE. Thus, the relaxation towards equilibrium is solely determined by the scattering term.

$$\left. \frac{\partial N_i}{\partial t} \right|_{\text{scatt}} = \frac{\partial N_i}{\partial t} \quad (3.5)$$

Following the approach of Woodruff and others [35, 42], we employ the relaxation time approximation to describe the scattering term as decay of N_i towards a Bose-Einstein distribution, N'_{i0} , at a modulated local temperature, $T' = T + \Delta T$.

$$\frac{\partial N_i}{\partial t} = \frac{N_i - N'_{i0}}{\tau} \quad (3.6)$$

where

$$N'_{i0} = (e^{\hbar\omega_i/k_B T'} - 1)^{-1} \quad (3.7)$$

and τ is the phonon lifetime, the average time between phonon collisions. The mode-specific time constants, τ_i , are not all available, so we make the practical assumption that τ is the same for all acoustic modes. Figure 3.4 outlines the perturbation theory and the corresponding dissipative relaxation.

3.4 Phonon BTE Solution

Solving BTE assuming plane wave solutions, $\Delta\omega_i, \Delta n_i, \Delta T \propto \exp(i(\mathbf{K} \cdot \mathbf{r} - \Omega t))$, yields

$$\Delta n_i = \omega_{i0} \left(\frac{\partial N'_{i0}}{\partial \omega_i} \right)_0 \left(\frac{\Delta\omega_i}{\omega_{i0}} - \frac{\Delta T}{T} \right) (1 - i\Omega\tau)^{-1} \quad (3.8)$$

The partial derivative can be evaluated as follows

$$\left(\frac{\partial N'_{i0}}{\partial \omega_i} \right)_0 = \frac{\partial}{\partial \omega_i} \left(\frac{1}{e^{\hbar\omega_i/k_B T'} - 1} \right)_0 = -\frac{\hbar e^{\hbar\omega_{i0}/k_B T}}{k_B T^2 (e^{\hbar\omega_{i0}/k_B T'} - 1)^2} \quad (3.9)$$

Since N'_{i0} is a function of $\frac{\omega_i}{T'}$, we can write the above derivative with respect to T' .

Evaluating the derivative with respect to T' gives

$$\left(\frac{\partial N'_{i0}}{\partial T'} \right)_0 = \frac{\partial}{\partial T'} \left(\frac{1}{e^{\hbar\omega_i/k_B T'} - 1} \right)_0 = \frac{\hbar\omega_{i0} e^{\hbar\omega_{i0}/k_B T}}{k_B T (e^{\hbar\omega_{i0}/k_B T'} - 1)^2} \quad (3.10)$$

and we see that

$$\left(\frac{\partial N'_{i0}}{\partial \omega_i} \right)_0 = -\frac{T}{\omega_{i0}} \left(\frac{\partial N'_{i0}}{\partial T'} \right)_0 = -\frac{T}{\omega_{i0}} \frac{C_{k,i}}{\hbar\omega_{i0}} \quad (3.11)$$

where $C_{k,i}$ is the specific heat contribution from a particular phonon mode that depends on the branch, i , and the phonon wavevector, k . The second equality follows from the definition of the specific heat due to acoustic phonons as the partial derivative of the phonon energy with respect to temperature. It can be written explicitly as

$$C_{k,i} = \frac{(\hbar\omega_{i0})^2 e^{\hbar\omega_i/k_B T}}{k_b T^2 (e^{\hbar\omega_{i0}/k_B T} - 1)^2} \quad (3.12)$$

and is related to the classical specific heat per unit volume using

$$C_v = \sum_{k,i} C_{k,i} \quad (3.13)$$

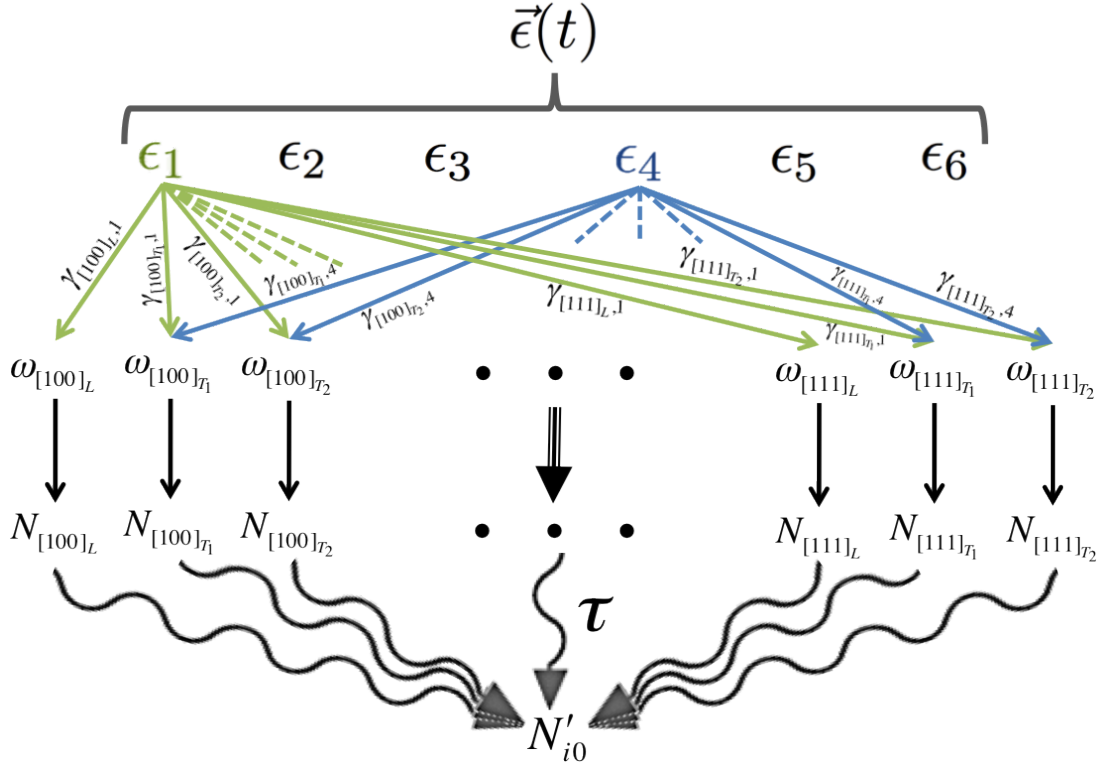


Figure 3.4: Overview of the energy loss due to anharmonic phonon-phonon scattering. Strain in one of the normal directions ϵ_{1-3} leads to a perturbation of phonon frequencies in each branch, characterized by the mode-Grüneisen parameter $\gamma_{i,j}$, where j is the strain direction and i represents the crystal direction and polarization. For the diamond lattice, we can express i using the notation $[hkl]_P$, where $[hkl]$ is a particular crystal direction (expressed using Miller indices) and P is the polarization, which can be either longitudinal (L) or transverse (T_1 or T_2). The modulation of phonon frequencies (and energies) means the respective branch populations are out of equilibrium. Each branch distribution relaxes towards the perturbed equilibrium distribution via phonon-phonon scattering. The energy loss that occurs during this irreversible relaxation process is assumed to come from the acoustic wave, because that is the source of the perturbation. The shear strains ϵ_{4-6} , however, perturb fewer phonon branches due to the restriction that volume is preserved.

where the subscripts indicate a summation over all acoustic phonon modes, specified by k and i .

After evaluating the partial derivative and combining terms we have

$$\Delta n_i = \left(-\frac{TC_{k,i}}{\hbar\omega_{i0}} \right) \left(\frac{\Delta\omega_i}{\omega_{i0}} - \frac{\Delta T}{T} \right) (1 - i\Omega\tau)^{-1} \quad (3.14)$$

For clarity, we proceed with the remainder of the derivation assuming uniaxial strain (i.e., $\vec{\epsilon}(t) = \epsilon_j$). We will show later how to make the appropriate modifications to capture the effect in realistically achievable vibration modes where Poisson contraction leads to deformation of more than one strain component. Under this uniaxial assumption, equation 3.2 reduces to

$$\frac{\Delta\omega_i}{\omega_{i0}} = \gamma_{i,j}\epsilon(t) \quad (3.15)$$

because ϵ_j is the only nonzero strain component so that only the j^{th} component of $\vec{\gamma}_i$ (indicated by the second subscript) contributes to the anharmonicity. As shown by Akhiezer, the temperature modulation can be determined self-consistently using the condition that the collision process conserve energy to first order [33, 42], giving

$$\frac{\Delta T}{T} = \sum_{k,i} C_{k,i} \frac{\Delta\omega_i}{\omega_{i0}} (1 - i\Omega\tau)^{-1} \bigg/ \sum_{k,i} C_{k,i} (1 - i\Omega\tau)^{-1} \quad (3.16)$$

We can express this succinctly as

$$\frac{\Delta T}{T} = \langle \gamma_{i,j} \rangle \epsilon(t) \quad (3.17)$$

where $\langle \gamma_{i,j} \rangle$ is the average of the j^{th} component of each $\vec{\gamma}_i$, weighted by its contribution to the total specific heat, over all phonon branches. Substituting equations 3.15 and 3.17 into the solution to the BTE gives

$$\Delta n_i = \left(-\frac{TC_{k,i}}{\hbar\omega_{i0}} \right) (\gamma_{i,j} - \langle \gamma_{i,j} \rangle) \epsilon(t) (1 - i\Omega\tau)^{-1} \quad (3.18)$$

3.5 Energy Loss

Now, we can proceed with the energy loss calculation. The energy loss per cycle of oscillation is simply the time average of the rate at which energy is lost via phonon-phonon scattering,

$$U_{loss/cycle} = - \sum_{k,i} \left\langle H_i \left(\frac{\partial N_i}{\partial t} \right)_{scatt} \right\rangle_{cycle} \quad (3.19)$$

where the $H_i = \hbar\omega_i$, is the phonon Hamiltonian and $\langle \cdot \rangle_{cycle}$ denotes the time average over one period of the mechanical vibration, $2\pi/\Omega$. We can rewrite this using the chain rule for derivatives,

$$U_{loss/cycle} = - \sum_{k,i} \left\langle N_i \frac{\partial H_i}{\partial t} - \frac{\partial(N_i H_i)}{\partial t} \right\rangle_{cycle} \quad (3.20)$$

The second term is simply the time derivative of the total energy, which we can eliminate because it must be constant in time. Due to the time average over one cycle, only the time-harmonic component of N_i contributes to the loss, so we can ignore N_{i0} and write

$$U_{loss/cycle} = - \sum_{k,i} \left\langle \Delta n_i \frac{\partial H_i}{\partial t} \right\rangle_{cycle} \quad (3.21)$$

Substituting the solution to the BTE in equation 3.18 and evaluating the derivative yields

$$U_{loss/cycle} = - \sum_{k,i} TC_{k,i} \frac{\gamma_i(\gamma_i - \langle \gamma_{i,j} \rangle)}{1 - i\Omega\tau} i\Omega \langle \epsilon^2(t) \rangle_{cycle} \quad (3.22)$$

after removing the time-independent terms from the $\langle \cdot \rangle_{cycle}$ brackets. Noticing that $\langle \epsilon^2(t) \rangle_{cycle} = \frac{\pi}{\Omega} \epsilon_0^2$, where ϵ_0 is the amplitude of the strain wave, and taking the real part of the energy loss reduces this to

$$U_{loss/cycle} = \sum_{k,i} TC_{k,i} (\gamma_{i,j}^2 - \gamma_{i,j} \langle \gamma_{i,j} \rangle) \pi \epsilon_0^2 \frac{\Omega\tau}{1 + \Omega^2\tau^2} \quad (3.23)$$

Assuming each branch contributes equally to the total phonon specific heat, we can eliminate the cumbersome summation and express the energy loss as

$$U_{loss/cycle} = \pi (\langle \gamma_{i,j}^2 \rangle - \langle \gamma_{i,j} \rangle^2) C_v T \epsilon_0^2 \frac{\Omega\tau}{1 + \Omega^2\tau^2} \quad (3.24)$$

where the angle brackets indicate an average over all phonon branches.

The energy loss expression has a few important features that merit discussion. First, we see that the dissipation is proportional to ϵ_0^2 as expected because energy loss should result regardless of whether the solid is in tension or compression. The loss is proportional to $\langle \gamma_{i,j}^2 \rangle - \langle \gamma_{i,j} \rangle^2$, which is reflective of the fact that each acoustic phonon branch relaxes not towards the ambient thermal equilibrium but instead towards a perturbed equilibrium determined by the average perturbation among all phonon branches. Finally, the frequency dependence is quadratic (or Lorentzian) so that the maximum loss occurs when $\Omega = 1/\tau$. Essentially, the energy loss is resonant with the relaxation rate ($1/\tau$). As the frequency of the elastic wave deviates from $1/\tau$ in either direction, the energy loss is reduced. This is a fundamental consequence of the fact that the instantaneous phonon distributions lag behind the (perturbed) equilibrium distribution because phonons can only relax towards this distribution via phonon-phonon scattering. The result matches Zener's phenomenological form for anelastic relaxation in solids, despite the fact that we have used the phonon BTE to solve for the energy loss, rather than Zener's generalized, anelastic stress-strain relation [41]. This similarity is expected because both formulations are based on a lag between either stress and strain or phonon populations and strain.

The simplicity of the uniaxial loss expression in equation 3.24 is quite useful for explaining the fundamental physics behind the anharmonic Akhiezer damping; however, real deformations in MEMS resonators are not uniaxial. Application of stress in one direction will result in Poisson contraction of the solid in the remaining two directions due to the crystal lattice structure. The dot product in the formulation of the phonon frequency perturbation in equation 3.2 shows that the phonon perturbation has a non-trivial dependence on the ratio of the six possible strain directions. Propagating this dot product through the energy loss

derivation leads to the following expression for mode-dependent energy loss

$$U_{loss/cycle} = \pi \Gamma_a^2 C_v T \frac{\Omega \tau}{1 + \Omega^2 \tau^2} \quad (3.25)$$

where we have used the newly defined anharmonic Grüneisen parameter

$$\Gamma_a^2 = \frac{\sum_i [(\vec{\gamma}_i - \langle \vec{\gamma}_i \rangle) \cdot \vec{\epsilon}] \cdot [\vec{\gamma}_i \cdot \vec{\epsilon}]}{n} \quad (3.26)$$

The time dependence of the strain $\epsilon(\vec{t})$ has been dropped due to the time averaging of the energy loss over one vibration cycle. Effectively, $\vec{\epsilon}$ can be considered as the strain vector under maximum deflection, when the potential energy storage is greatest. In this expression, the left term in rectangular brackets describes the relaxation of the phonon branch distributions from their individual perturbations towards the average distribution and the right term in rectangular brackets describes the perturbation of the phonon energies themselves. We note that the perturbation of the average distribution is also strain dependent and can be expressed as

$$\langle \vec{\gamma}_i \rangle = \frac{\sum_i \vec{\gamma}_i \cdot \vec{\epsilon}}{n} \quad (3.27)$$

where n is the number of acoustic phonon branches and we have again assumed that each branch contributes equally to the total phonon specific heat. We note that the anharmonic Grüneisen parameter, Γ_a^2 is scalar-valued, as we expect since the energy loss must be a scalar. Thus, the dot products and summations in the expression for Γ_a^2 can be expanded to give an expression that is free of vector products; however, due to the large number of phonon branches, this expanded form would have over a thousand terms, which is not conducive towards evaluation so we do not display the expression in this linear form.

3.6 Mode-Grüneisen Parameters and Third Order Elastic Moduli

If the second-order elastic coefficients (SOEC) and third-order elastic coefficients (TOEC) are known, theoretical values for $\gamma_{i,j}$ can be obtained and the energy loss expression can be calculated using only bulk parameters. The mode-Grüneisen parameters are determined as ratios of second-order and third-order elastic moduli [49] as follows

$$\gamma_i^{jk} = -\frac{1}{2c_i} [2c_i U_j U_k + c_{jkmn} N_m N_n + C_{jkmunv} N_m N_n U_u U_v] \quad (3.28)$$

and

$$c_i = c_{abcd} N_a N_c U_b U_d = \sum_a \sum_b \sum_c \sum_d c_{abcd} N_a N_c U_b U_d \quad (3.29)$$

where N_q are the direction cosines to the propagation direction, U_q are the direction cosines to the polarization direction, c_{jkmn} are the SOECs, C_{jkmunv} are the TOECs and repeated indices indicate a summation over that index (in accordance with Einstein's notation for tensors).

The above expression represents a generalization of thermal expansion coefficients that includes anharmonicity along different crystal directions [37]. The average Grüneisen parameter is $\gamma_0 = 3\alpha_L B/C_v$ where α_L is the linear thermal expansion coefficient, $B = \rho c^2$ is the bulk modulus and C_v is the specific heat per unit volume. Macroscopically, thermal expansion relates the deformation (strain) that results when the solid is heated due to an increase in ambient temperature, so it will be isotropic; however, if we consider the reverse case, i.e., modulation of the internal temperature (phonon energies) of the solid due to an applied strain, we see that the local 'heating' (increase or decrease in the phonon energies $\hbar\omega$) is anharmonic. This fact is confirmed by the formulation of the perturbation theory. Multiplying 3.2 by \hbar , converting it to a perturbation of phonon energies rather than frequencies, and taking the partial derivative of equation with respect to the

strain gives

$$\gamma_{i,j} = -\frac{\partial(\hbar\omega_i)}{\partial\epsilon_j}/(\hbar\omega_{i0}) \quad (3.30)$$

and we see the at the mode-Grüneisen parameter represents the relative strength of the acoustic phonon energy perturbation for different phonon branches. Since acoustic phonons represent collective vibrations of the atoms in a crystal, their energy is kinetic energy and can be interpreted as local ‘phonon’ temperature.

In order to properly evaluate the mode-Grüneisen parameters, we must consider the strain (jk) as a second-order tensor (3x3), the SOECs as a fourth-order tensor and the TOECs as a sixth-order tensor. Each index (excluding i , indicating the direction and polarization of the acoustic phonon mode) can take a value of 1, 2 or 3 corresponding to the x-, y- and z-directions, respectively, in the Cartesian coordinate system. Each pair of indices corresponds to a strain direction for orthotropic crystals. We use the conventional mapping: 11 \rightarrow 1; 22 \rightarrow 2; 33 \rightarrow 3; 23, 32 \rightarrow 4; 13, 31 \rightarrow 5; 12, 21 \rightarrow 6 where the symmetry of the cubic-point group dictates that $jk \leftrightarrow kj$.

The fourth-order tensor of SOECs has three independent coefficients: $c_{1111} \rightarrow c_{11}$, $c_{1122} \rightarrow c_{12}$, and $c_{2323} \rightarrow c_{44}$. The rest of the tensor can be populated by noting the symmetry of the cubic crystal. The c_{jjjj} , coefficients are all equal, the poisson contraction terms c_{jjkk} are equal and the equivalence of shear direction implies c_{jkkj} with $j \neq k$ are equal. Swapping the pairs of indices gives the same value of the coefficient. The remaining terms, which represent the coupling among shear modes (for example c_{jklj}) are all zero. We note that these three components can also expressed in terms of the two Lamé coefficients λ and μ where $c_{12} = \lambda$, $c_{44} = \mu$ and $c_{11} = 2\mu + \lambda$; however that formulation is not conducive to evaluation of equation 3.28.

The sixth-order tensor of TOECs are comprised of six independent coefficients: $C_{111111} \rightarrow C_{111}$, $C_{111122} \rightarrow C_{112}$, $C_{112233} \rightarrow C_{123}$, $C_{112323} \rightarrow C_{144}$, $C_{111212} \rightarrow C_{166}$, and $C_{231312} \rightarrow C_{456}$. The remaining terms in the sixth-order tensor can

be populated using the same rules detailed above for the fourth-order tensor of SOECs.

Mason and Bateman establish that the mode-Grüneisen parameters are ratios of TOECs to SOECs and calculate $\gamma_{i,1}$ and $\gamma_{i,5}$ for silicon and germanium [34]. Critically, they show that $\langle \gamma_{i,1} \rangle \approx \gamma_0$ as expected, because both averages relate to volume perturbation of the solid. They also verify that $\langle \gamma_{i,5} \rangle = 0$, which satisfies the restriction that shear deformations do not perturb volume.

3.7 Summary

In this chapter, a rigorous derivation of the anharmonic phonon-phonon dissipation using the Boltzmann transport equation has been presented. We dispense with Woodruff's cursory assumption that all phonon modes are perturbed identically (by the average Grüneisen parameter γ_0) and the anharmonicity among phonon modes has been included by incorporating the mode-Grüneisen parameters, which are evaluated using the second and third-order elastic coefficients. The derivation reveals that anharmonicity is the origin of the dissipation (even for the uniaxial case), which implies that Woodruff's isotropic scheme is fundamentally flawed and obscures the fundamental physics behind the Akhiezer loss. Additionally, the physical significance of the mode-Grüneisen parameters has been discussed in detail. The following chapter focuses on evaluation of the quality factor, which is a ratio of energy stored to energy lost per cycle, for common vibration modes in planar silicon resonators.

CHAPTER 4

Quality Factor

4.1 Mode- and Orientation-Dependent Energy Storage

The quality factor is a ratio of energy stored to energy lost per cycle, so it is important to account for the anisotropy and mode-dependence in both. For cubic crystals, the energy storage is anisotropic and depends on the deformation profile or vibrational mode shape. The elasticity of the crystal can be described by relating stress ($\vec{\sigma}$) and strain ($\vec{\epsilon}$) using the second-order elastic tensor.


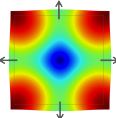
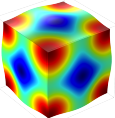
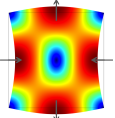
$$\vec{\sigma} = \begin{bmatrix} c_{11} & c_{12} & c_{12} & 0 & 0 & 0 \\ c_{12} & c_{11} & c_{12} & 0 & 0 & 0 \\ c_{12} & c_{12} & c_{11} & 0 & 0 & 0 \\ 0 & 0 & 0 & c_{44} & 0 & 0 \\ 0 & 0 & 0 & 0 & c_{44} & 0 \\ 0 & 0 & 0 & 0 & 0 & c_{44} \end{bmatrix} \cdot \vec{\epsilon} \quad (4.1)$$

Here, appropriate simplifications have been made given cubic symmetry and the equivalence of shear directions, so that the elasticity matrix can be described using only three components c_{11} , c_{12} and c_{44} .

For a given vibration mode and orientation, the energy stored is a scalar so that an effective Young's modulus or storage modulus, E_{eff} , can be defined so that the energy storage per unit volume is $E_{stored} = \frac{1}{2}E_{eff}\epsilon_0^2$ [50]. For spatially uniform modes, we can eliminate the integral over the volume of the structure, because the energy storage (and loss) in any volume element of the solid is the same.

For analytical evaluation, the effective Young's moduli are determined assuming infinite geometries (i.e., the resonator size does not affect the resulting strain profile). A stress profile is applied to the infinite solid and the resulting strain is calculated using the matrix equation above. For example, we can apply a uniaxial stress in the x-direction (σ_1) and use the orthotropic stress-strain relationship to determine the resulting deformation in the x, y and z-directions. Normal stress in a single direction will lead to deformation in all three normal directions, while the shear strains are uncoupled due the sparse nature of the elasticity matrix. The modes of interest are width-extensional (WE), square-extensional (SE), cubic-extensional (CE) and Lamé; their deformation profiles and expressions for effective storage moduli are given in Table 4.1. These are commonly used vibration modes for a single-crystal rectangular parallelepiped with edges oriented along the [100] axes. The WE, SE and CE modes are modes where the deformation of the solid is primarily due to extension (and contraction) along one, two or three principal axes, respectively. The Lamé mode (also called a 'contour' mode) is a pure shear mode with only one nonzero strain component.

Table 4.1: Displacement profiles and elastic storage moduli for common vibration modes of a single-crystal rectangular parallelepiped with edges oriented along the [100] directions.

Width- Extensional	Square- Extensional	Cubic- Extensional	Lamé (shear)
			
$\frac{(c_{11}-c_{12})(c_{11}+2c_{12})}{c_{11}+c_{12}}$	$c_{11} + c_{12} - \frac{2c_{12}^2}{c_{11}}$	$\frac{c_{11}+2c_{12}}{3}$	c_{44}

4.2 Quality Factor

Using the definition of the quality factor, the energy storage expression in the previous section and the energy loss in equation 3.24 we can write the quality factor as,

$$Q = \frac{E_{eff}}{(\langle \gamma_{i,j}^2 \rangle - \langle \gamma_{i,j} \rangle^2) C_v T} \frac{1 + \Omega^2 \tau^2}{\Omega \tau} \quad (4.2)$$

for the uniaxial case. If we employ Woodruff's simplifications that the material is isotropic so all $\gamma_{i,j} = \gamma_0$ and that $\Delta T = 0$, and assume the storage modulus is simply the bulk modulus, $B = \rho c^2$, this expression reduces identically to equation 3.1 in the low-frequency limit. This result is expected because both methods use the BTE to determine the energy loss. Woodruff's assumptions allow for simple estimation of Q using bulk material data, but it is important to note that these assumptions are not self-consistent. If the material is assumed to be isotropic and all $\gamma_{i,j} = \gamma_0$, then the average $\langle \gamma_{i,j} \rangle = \gamma_0$ which implies that $\Delta T \neq 0$. In fact, when this assumption is employed rigorously, $\langle \gamma_{i,j}^2 \rangle = \langle \gamma_{i,j} \rangle^2 = \gamma_0^2$ and the dissipation in equation 3.24 is zero. We also note that the result derived here does in fact match Zener's expression for quality factor due to anelastic relaxations in a solid. This suggests that Mason's method can also be used to obtain the same result, although we do not include it here [51]. Briefly, Mason's simplification is approximately valid in the low-temperature limit, where the upper integration limit in the Debye integral approaches infinity and the assumption that the integration limits are strain-independent is satisfied. In this low-temperature limit, the total acoustic phonon energy $U_0 \approx C_v T/4$. This is precisely the condition that reveals the T^3 dependence of the low-temperature Debye specific heat in insulators [37]. This likely explains the persistent deviation from experimental values at high temperatures when employing modified versions of Mason's expression for acoustic attenuation [43]. Even if these low-temperature conditions are satisfied, Mason's expression omits a factor of 4, which is produced when proper care is

taken to include the strain-dependence of all phonon frequency terms [42].

Now, including the mode-dependent energy loss expression in equation 3.25 we can write the mode-dependent quality factor

$$Q = \frac{E_{eff}}{\Gamma_a^2 C_v T} \frac{1 + \Omega^2 \tau^2}{\Omega \tau} \quad (4.3)$$

where

$$\Gamma_a^2 = \sum_i [(\vec{\gamma}_i - \langle \vec{\gamma}_i \rangle) \cdot \vec{\epsilon}] \cdot [\vec{\gamma}_i \cdot \vec{\epsilon}] / n \quad (4.4)$$

Here Γ_a^2 represents the strength of the phonon frequency perturbation. In the above expression, we have included the mode-dependent energy and storage, as well as the anharmonicity among phonon modes that results even for the uniaxial case. A summary of the key differences between Woodruff's isotropic expression and the anharmonic expression derived in this work is given in figure 4.1.

$Q = \frac{\overline{\rho c^2}}{\gamma_0^2 C_v T} \frac{1}{\Omega \tau}$ <p>(Woodruff, 1961)</p>	<div style="border: 1px dashed black; padding: 5px; display: inline-block;"> $Q = \frac{\overline{E_{eff}}}{\Gamma_a^2 C_v T} \frac{1 + \Omega^2 \tau^2}{\Omega \tau}$ </div>	
Bulk Modulus (ρc^2)	Energy storage	Anisotropic Young's Modulus (E_{eff})
✗	Mode-dependent energy storage	✓
Inverse	Frequency (Ω) Dependence	Quadratic
✗	Zener's form for anelastic relaxations	✓
✗	Anharmonicity	✓
✗	Mode-dependent phonon perturbation	✓
✗	Applies to shear modes	✓

Figure 4.1: Woodruff's isotropic expression compared with the rigorous anharmonic expression derived in this work. Our expression correctly incorporates mode- and orientation-dependent energy storage, parabolic frequency dependence due to the lag between the strain and the phonon distributions, and the anharmonic phonon perturbation, which is mode-dependent. Our anharmonic Q can be applied to all uniform modes given the strain vector $\vec{\epsilon}$.

4.3 Analytical Results

In this section, we evaluate the quality factor limits in silicon and compare the performance for common vibration modes. The final parameter needed to evaluate Q is the phonon lifetime, τ . Following Woodruff's approach, we determine τ using the definition of bulk thermal conductivity, $\kappa \equiv \frac{1}{3}C_v c^2 \tau$. This is, in effect, an average time constant over all phonon branches. Others have replaced the average phonon time constant τ with the direction-specific lifetimes $\tau_{[hkl]}$ corresponding to the particular crystal orientation of the mechanical vibration [52, 53], but we assert that this is not the most accurate approach, because the strain perturbs phonon branches in *all* crystal directions, not just along the direction of sound propagation, making a collective relaxation time a better estimate. The most accurate approach would be to use the branch-specific τ_i , which depend on both direction and polarization; however, lack of a complete set of experimental values for these time constants prohibits calculation in this way.

Figure 4.2 shows the room temperature $f \times Q$ product as a function of the mechanical resonant frequency for the WE, SE, CE and Lamé modes of a resonator with edges oriented along the [100] directions in intrinsic silicon evaluated using the expression in equation 4.3 along with Woodruff's result for reference and a number of experimental results from silicon resonators in the literature [54–67]. As expected, given the quadratic dependence of Q on resonant frequency in the Zener model, the curves remain constant up to ~ 20.5 GHz, corresponding to the condition $\Omega\tau = 1$. Again, we note that the Akhiezer damping model only applies when $\Omega \ll 1/\tau$, so the results should only be interpreted below this value; at higher frequencies, the strain varies faster than the phonon scattering rate, so the number of average collisions per cycle is severely reduced and an alternate model, often called Landau-Rumer dissipation, should be used instead [68]. We can equivalently express this condition as $l_{ph} \ll \lambda_{ac}$, where l_{ph} is the mean-

free-path for thermal phonons and λ_{ac} is the wavelength of the elastic wave. As a result, we can reframe the frequency cutoff as a minimum size limitation. A simple calculation (ignoring phonon dispersion) gives $l_{ph} \approx 47 \text{ nm}$ for silicon at room temperature. This means our damping model provides a valid picture of the phonon-phonon dynamics for resonators where all dimensions are greater than $\sim 47 \text{ nm}$, which serves as a theoretical minimum cutoff size for bulk phonon phenomena in single-crystal silicon at room temperature. We note, however, that Ju and Goodson report average phonon mean-free-paths of $\sim 300 \text{ nm}$ in thin silicon layers via thermal conductivity measurements [69] and more recent work provides evidence of a broad spectrum of phonon mean-free-paths in silicon, where phonons with $l_{ph} > 1 \mu\text{m}$ contribute significantly to the thermal conductivity [70, 71].

The (solid) theory curves show that the upper limit on Q for the WE mode is greater than that of SE mode, which is, in turn, larger than the CE mode. This result can be inferred from the anharmonic Grüneisen parameter, Γ_a^2 , derived in Section 3.4. In the WE mode, the structure expands in the x-direction and contracts in both the y- and z- directions due to the Poisson ratio; as a result, the dissipation is reduced compared to the uniaxial strain case. In the SE mode, the solid expands in x and y (and contracts in z) so that the deformation of the mechanical mode resists the natural contraction of the solid. The perturbations of x and y add constructively, leading to increased dissipation compared to the WE mode. This leads to reduced Q despite the fact that the SE mode has a higher energy storage density than the WE mode. In the CE mode, the solid expands in the x-, y- and z-directions resulting in the largest combined perturbation and energy dissipation and the smallest Q . Our results indicate that the quality factor limits for silicon at a specified resonant frequency can vary widely when including anisotropic energy storage and loss ($Q_{Lamè} : Q_{WE} : Q_{SE} : Q_{CE}$ equals 4.3 : 1.5 : 1.3 : 1).

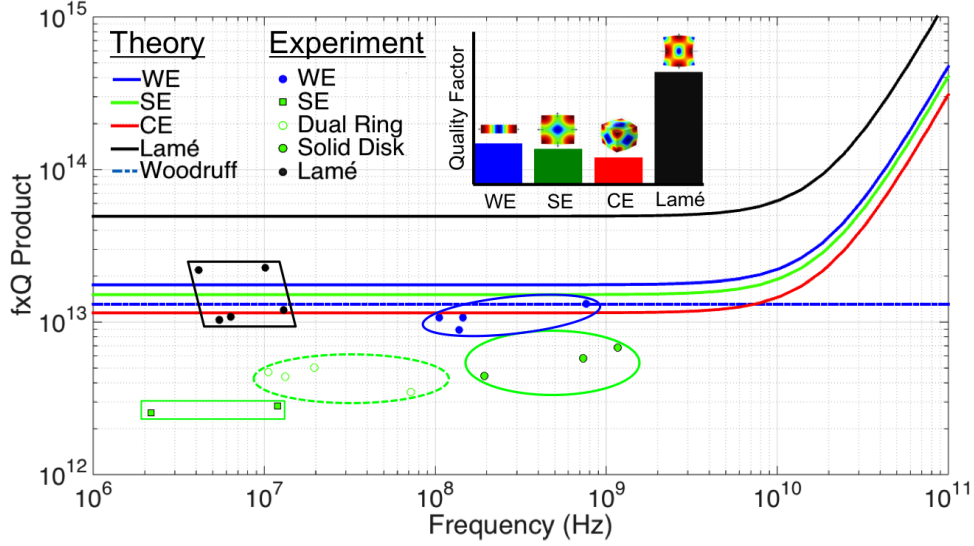


Figure 4.2: Anharmonic and anisotropic $f \times Q$ product limits vs. mechanical resonant frequency at room temperature for WE, SE, CE and Lamé modes in [100] silicon. The solid lines represent the quality factor limits derived in this work (equation 4.3). The dashed line is Woodruff’s estimation of the Akhiezer damping limit and the points are experimental results from high quality factor resonators surveyed from the literature [54–67]. A number of recently fabricated resonators have quality factors that exceed Woodruff’s limit, indicating that the simplified, isotropic expression does not provide sufficient accuracy.

The Lamé mode has the highest upper bound on Q for the modes considered in this work, despite having the smallest energy storage modulus. This is an important consequence of the condition that shear vibrations modes preserve volume. In a pure shear vibration, the mode-Grüneisen parameters for longitudinal phonon branches do not contribute, because these perturbations would change the volume of the solid. Effectively, the phonon-phonon scattering for shear vibrations is limited to the volume-preserving phonon branches, which leads to reduced energy dissipation because fewer branches, and less phonon energy, are subject to the relaxation process. This is evident from calculation of the mode-Grüneisen pa-

rameters, of which only 18 of 39 are non-zero for a shear-mode perturbation. This result indicates that Lamé mode resonators may be the best candidates for ultra high Q silicon resonators. We note that Woodruff’s isotropic formula actually predicts infinite Q (zero dissipation) for shear modes because the average Grüneisen parameter (γ_0 in equation 3.1) for volume-preserving modes is zero. The limitations of Woodruff’s expression have been acknowledged in the past [42, 46], but we are the first to provide a viable alternative expression that shows that shear mode vibrations do in fact lead to anharmonic phonon-phonon dissipation.

The evaluation of the anharmonic and anisotropic expression derived in this work indicates that Woodruff’s order-of-magnitude result (dashed line) fails to provide an upper bound on quality factor due to Akhiezer damping. In fact, several silicon resonators with quality factors that exceed Woodruff’s limit have already been fabricated and measured in the literature [54–57], indicating the important need for our more accurate damping model that provides a robust upper bound on the performance of modern micromechanical resonators.

The experimental points are broadly categorized by geometry and mode type. The highest Q resonators of a given type are grouped horizontally, reinforcing the assertion that the $f \times Q$ product is constant for a particular mode shape, in accordance with Equation 4.3. It is important to convey the fact that evaluation of Equation 4.3 provides an upper bound on the quality factor, so it only predicts the performance of devices that are limited by anharmonic phonon-phonon dissipation, meaning other loss mechanisms including TED, air-damping and anchor loss have insignificant contributions. We also note that the theory lines in Figure 4.2 use the idealized mode profiles in Table 4.1, and, consequently, do not necessarily predict the exact behavior of the devices included as experimental references, because the actual vibrational modes are complicated functions of the geometry and boundary conditions of the structure. Additionally, the results here are for intrinsic silicon, and do not account for variations due to dopant species and density.

The most accurate results can be obtained if the doping dependencies of second- and third-order elastic coefficients and thermal conductivity, which determines τ , are known [72].

CHAPTER 5

Finite Element Modeling

The Akhiezer damping limit presented in the previous chapter uses idealized vibrational mode-shapes assuming an infinite solid. These simple deformations can be solved for analytically assuming in-phase stimuli (i.e., hydrostatic pressure) and calculating the resulting strain profile given the elasticity matrix that relates stress and strain. Even these simple geometries have intricate expressions for the effective energy storage moduli as given in Table 4.1. While these are good estimates for first-order modes for simple geometries, many modern MEMS devices have complex, 3-D geometries and are actuated in higher-order vibrational modes. Complex geometries are often employed to reduce TED and anchor loss and high-order modes are used to achieve higher frequency operation (i.e., for radio-frequency applications). These complex mode shapes are extremely difficult, if not impossible, to solve for analytically. Finite element analysis, on the other hand, provides a method to solve for these complex eigenmodes and has been used successfully to predict the resonant frequencies of MEMS structures. Figure 5.1 shows three higher-order modes for a width-extensional bulk acoustic resonator (WEBAR) with a width of $30\mu m$, length of $150\mu m$ and thickness of $5\mu m$ from Pourkamali *et al.* [60]. These are three simulated modes for the exact same resonator. The simulated resonant frequencies for the three depicted modes are 142 MHz, 419 MHz and 664MHz and match well with the experimentally measured values of 144 MHz, 427 MHz and 764 MHz, respectively.

Complex geometries can be drawn using computer-aided design (CAD) method-

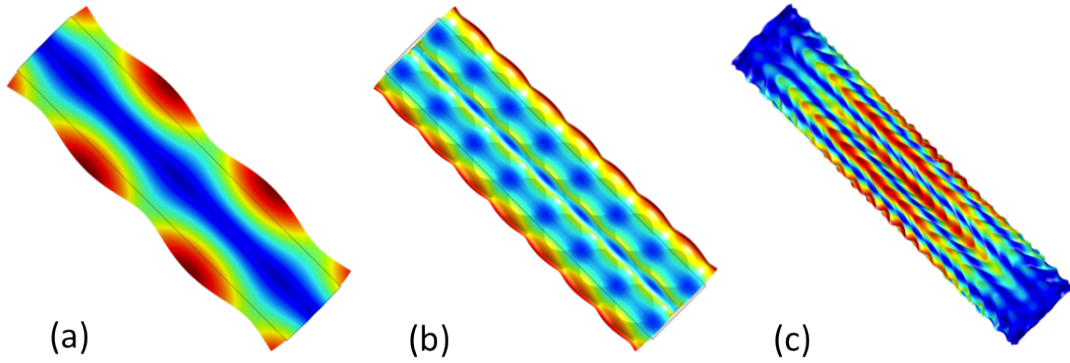


Figure 5.1: Finite element simulation (Comsol Multiphysics[®]) of higher-order modes of a $30\mu\text{m}$ wide, $150\mu\text{m}$ long and $5\mu\text{m}$ thick width extensional bulk acoustic resonator (WEBAR) from Pourkamali *et al.* [60]. (a) WEBAR mode with a simulated resonant frequency of 142MHz and measured frequency of 144MHz, (b) higher-order mode with simulated frequency of 419 MHz and measured frequency of 427 MHz, and (c) very complex higher-order mode with a simulated frequency of 664MHz and measured frequency of 764MHz. These modes are nearly impossible to solve for analytically, hence the need for finite element models in to predict both resonant frequency and energy dissipation limits.

ologies and non-trivial boundary conditions can be imposed on the structure in order to more accurately capture operation of the as-fabricated MEMS resonator. These include curved geometries, fixed and free boundary conditions, and tethers that anchor the device to the substrate. Additionally, finite element modeling solves for both the vibrational-mode and resonant frequency simultaneously so that only realizable modes are simulated, whereas the analytical result considers the vibrational mode and frequency separately. Thus, we can take advantage of powerful, commercially available finite element solvers in order to expand the applicability of the analytical Akhiezer damping formulation.

Finite element models (FEM) divide the solid into individual mesh elements (typically tetrahedrons) and use continuum mechanics with the appropriate bound-

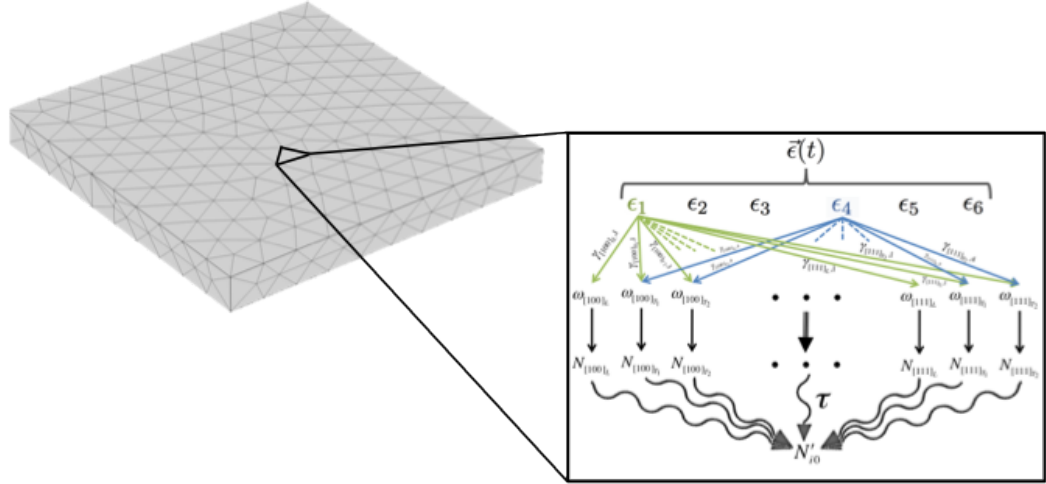


Figure 5.2: The analytical Akhiezer dissipation calculation is applied to each individual mesh element. The energy loss and energy storage is then integrated over the volume of the structure in order to evaluate the quality factor.

ary conditions in order to simulate the vibrational mode-shape. The result is an element-by-element matrix of the six strain components, assuming an orthotropic crystal. Essentially, we use the finite element model to solve for both the mechanical eigenmode and eigenfrequency and use the strain profile to calculate the energy loss and energy storage in each mesh element. This scheme is represented in figure 5.2. The storage and loss are then integrated over the volume of the structure and then combined appropriately to determine the overall Q . We use Comsol Multiphysics[®], a commonly used commercial FEM solver, to simulate the mechanical eigenmode, and perform the storage and loss calculations in Matlab[®]. The high-level implementation is given in figure 5.3.

Here, we present a step-by-step methodology for calculating the quality factor limit due to Akhiezer damping for silicon resonators using Comsol Multiphysics[®]

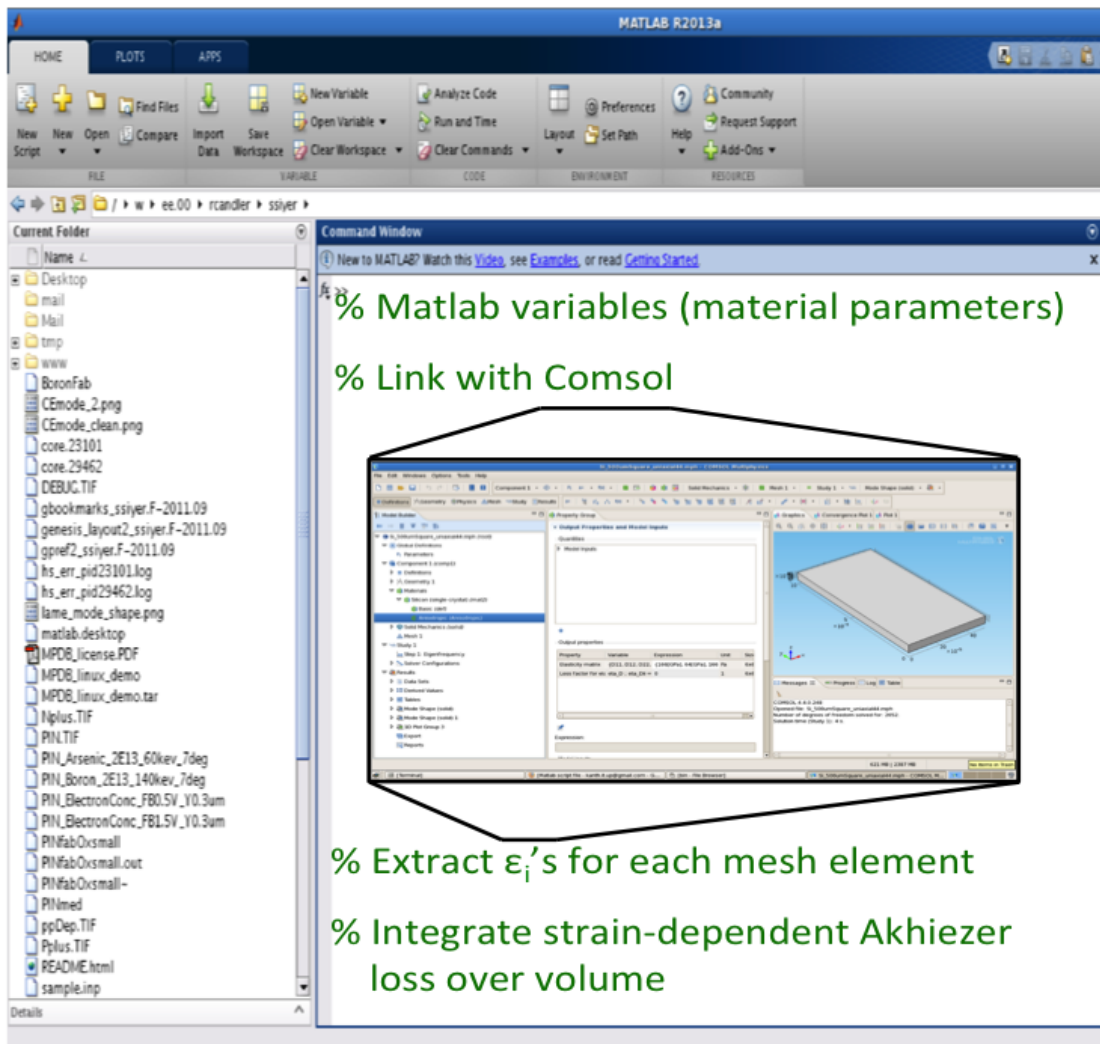


Figure 5.3: High-level picture of the implementation of the Akhiezer dissipation calculation with commercially available finite element software. Matlab[®] is used to apply the material parameters (namely second-order elastic moduli) to the finite element model (FEM), the anisotropic mechanical mode shape is then simulated with the FEM software, and finally the results are extracted back to Matlab[®] in order to calculate energy storage and energy loss due to Akhiezer damping.

and Matlab[®]. First, we will show how to set up the appropriate Comsol[®] simulation, then we will explain how the simulation data can be exported to a text file and then inputted into a Matlab[®] script to calculate both the energy storage and loss in order to evaluate Q . First, create a 3-D Comsol Multiphysics[®] model using the ‘Solid Mechanics’ physics module and adding the built-in ‘Eigenfrequency’ study. Next, draw the resonator geometry by using the built-in functions, or by importing a CAD file from another design tool. The Akhiezer damping model in this work assumes an anisotropic cubic crystal, so we must use an anisotropic material model for the elasticity of silicon. Add the built-in anisotropic silicon material model and select the anisotropic linear elastic material model. The elasticity matrix ‘D’ contains the second order elastic coefficients that relate stress and strain (see equation 4.1). The final set-up step is to add the appropriate boundary conditions including fixed or free faces, edges or points and symmetry constraints. Now, run the eigenfrequency simulation inputting an estimated resonant frequency of the desired vibration mode. Once the simulation is complete, select the appropriate mode shape. The results then can be exported to a text file, which will contain data for each mesh element. The required information is the eigenfrequency (‘solid.freq’), element volume (‘meshvol’) and the six strain components in the local strain tensor (‘solid.el11’, ‘solid.el22’, ‘solid.el33’, ‘solid.el23’, ‘solid.el13’, ‘solid.el12’). Use the Gauss point evaluation to ensure only one data point is exported for each element. Each row of the exported data file will contain the x, y and z components indicating the center point of the mesh element and the eight data values listed above for each element in the mesh. The exported data file contains all the required information to calculate the energy storage and energy loss in each mesh element and can be imported into Matlab[®] where analytical calculations can be performed.

The energy storage in each element is

$$E_{stored} = \frac{1}{2} \vec{\sigma} \cdot \vec{\epsilon} dV \quad (5.1)$$

where $\vec{\epsilon}$ is the strain vector from the exported data, $\vec{\sigma}$ is the stress vector which can be calculated from equation 4.1, and dV is the volume of the mesh element.

The energy loss calculation is more involved because the loss per cycle in each element itself will be a sum over the acoustic phonon branches and the loss expression in each branch will depend on the average mode-Grüneisen parameter (requiring yet another summation). The most straightforward approach is to first evaluate all the mode-Grüneisen parameters using equation 3.28 and evaluate the perturbation of each branch ($\Delta\omega_i/\omega_{i0}$) and average these to determine the perturbation of the internal temperature of the mesh element ($\Delta T/T$). Equation 3.28 depends on the branch index (i) and the strain direction (jk) indicating that each branch will have six mode-Grüneisen parameters. All six must be evaluated and combined into a single vector $\vec{\gamma}_i$. We note that, due to the symmetry of the cubic lattice, $\langle\gamma_i^{11}\rangle = \langle\gamma_i^{22}\rangle = \langle\gamma_i^{33}\rangle = \gamma_0^2$ and $\langle\gamma_i^{23}\rangle = \langle\gamma_i^{13}\rangle = \langle\gamma_i^{12}\rangle = 0$. Similarly, $\langle(\gamma_i^{11})^2\rangle = \langle(\gamma_i^{22})^2\rangle = \langle(\gamma_i^{33})^2\rangle$ and $\langle(\gamma_i^{23})^2\rangle = \langle(\gamma_i^{13})^2\rangle = \langle(\gamma_i^{12})^2\rangle$. The net perturbation of each branch due to strain in all six directions will be

$$\frac{\Delta\omega_i}{\omega_{i0}} = \vec{\gamma}_i \cdot \vec{\epsilon} \quad (5.2)$$

and the average perturbation among all phonon branches will be

$$\frac{\Delta T}{T} = \left\langle \frac{\Delta\omega_i}{\omega_{i0}} \right\rangle = \frac{1}{n} \sum_i \vec{\gamma}_i \cdot \vec{\epsilon} \quad (5.3)$$

where n is the number of acoustic phonon modes (39 in silicon). Now we can determine the energy loss per cycle due to the relaxation of a single phonon branch as

$$E_{loss/cycle,i} = \pi C_v T \frac{\Omega\tau}{1 + (\Omega\tau)^2} \frac{dV}{n} \left(\frac{\Delta\omega_i}{\omega_{i0}} - \frac{\Delta T}{T} \right) \cdot \frac{\Delta\omega_i}{\omega_{i0}} \quad (5.4)$$

Thus, the total energy loss in a mesh element due to all phonon branches is

$$E_{loss/cycle} = \sum_i E_{loss/cycle,i} = \pi C_v T \frac{\Omega \tau}{1 + (\Omega \tau)^2} \frac{dV}{n} \sum_i \left(\frac{\Delta \omega_i}{\omega_{i0}} - \frac{\Delta T}{T} \right) \cdot \frac{\Delta \omega_i}{\omega_{i0}} \quad (5.5)$$

The total energy storage will be the sum of the energy storage equation 5.1 over all mesh elements and the total energy loss will be the sum of equation 5.5 over all mesh elements. The quality factor can then be evaluated using its fundamental definition $Q = 2\pi \frac{E_{stored}}{E_{loss/cycle}}$.

Integration of the analytical Akhiezer damping model with FEM allows for a more accurate prediction of the quality factor for the experimental points given in Figure 4.2. In particular we focus on the three points that lie above Woodruff's isotropic limit [54, 60, 74]. The simulated results are presented in the bar chart in Figure 5.4. In this figure the green (dashed) line represents the fQ product limit due to Akhiezer damping and the (solid) black line is the measured fQ product. Within the bar with the solid black outline, the blue area indicates the fraction of the energy loss due to Akhiezer damping and the yellow area is the fraction due to other loss mechanisms. It is important to note that because the quality factors add inversely, if the Akhiezer-limited Q is twice the measured value that indicates that 50% of the energy loss is due to Akhiezer damping. Akhiezer damping is a dissipation limit, so that none of the devices have a measured Q that is larger than that predicted by the anharmonic phonon dissipation limit presented in this work. However, there are several devices reported in the literature where Akhiezer damping is the dominant loss mechanism.

The first three modes (a)-(c) in Figure 5.4 are the three higher-order modes of the width-extensional bulk acoustic resonator (WEBAR) with a width of $30\mu m$ x $150\mu m$ x $5\mu m$ from Pourkamali *et al.* [60] that are represented in Figure 5.1. The measured results are all from a single bar resonator so that variation among different resonators due to fabrication non-idealities is not a factor in the analysis

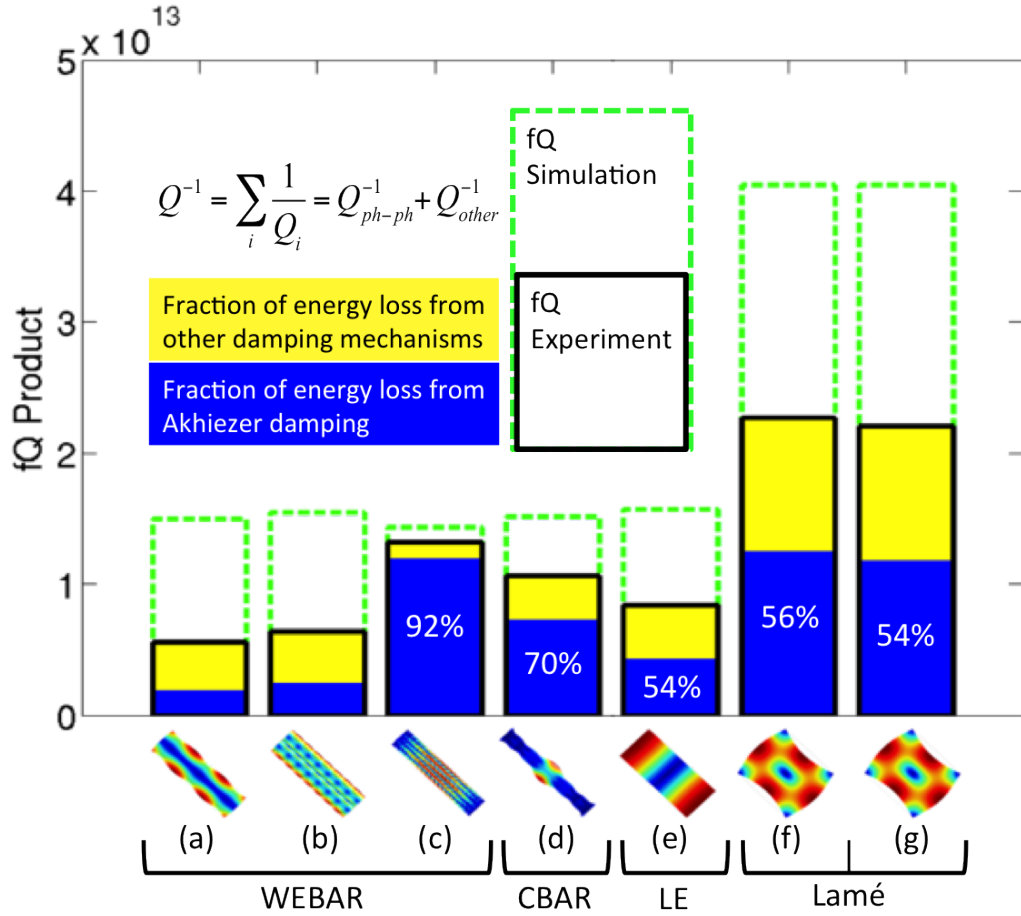


Figure 5.4: Simulated Akhiezer damping fQ versus experimentally measured fQ for several high- Q devices in the literature. The dashed green line is the fQ product limit due to Akhiezer damping and the solid black line is the measured fQ product. Within the solid block, the blue area is the fraction of the dissipation due to Akhiezer damping and the yellow area is the fraction due to other loss mechanisms. Q 's add inversely so an simulated Q that is twice the measured value indicates 50% of the loss is due to Akhiezer damping. (a)-(c) Three modes of the width-extensional bulk acoustic resonator (WEBAR) with a width of $30\mu m \times 150\mu m \times 5\mu m$ [60]. (d) A $400\mu m$ long concave bulk acoustic resonator (CBAR) where the center is narrower ($40\mu m$) than the end ($60\mu m$) [73]. (e) A length-extensional mode of a $600\mu m$ long, $20\mu m$ thick resonator, tethered at its center [74]. (f) $400\mu m \times 400\mu m \times 20\mu m$ Lamé mode resonator [74] (g) $1000\mu m \times 1000\mu m \times 46\mu m$ Lamé mode resonator [54].

of the dissipation in these modes. The results indicate that the measured Q varies widely for different modes, with the fQ product of the third-mode being over twice the value of the first mode. The most interesting result among these three modes is the fact that the energy loss is dominated by the Akhiezer effect with 92% of the of the dissipation due to anharmonic phonon scattering, as predicted by the model presented in this work. Thus, we can conclude that the device, operated in this mode, is extremely close to the intrinsic limit in silicon. We also note that the measured fQ is above Woodruff's isotropic limit, indicating the need for the new anharmonic limit presented in this work. The large difference in measured fQ for the first two modes versus the third mode seems to indicate that the remaining dissipation may be largely due to leakage of acoustic energy through the anchors, since the third mode (with higher fQ) has the elastic energy concentrated in the center, with a large nodal area near the tethers which anchor the device on the shorter (width) side of the WEBAR. The fourth mode (d) in Figure 5.4 is a concave bulk acoustic resonator (CBAR) fabricated and measured by Samarao *et al.* where the width at the center of the device is narrower than at the ends [73]. The center width is $40\mu m$ while the end width is $60\mu m$ with a length of $400\mu m$ and thickness of $20\mu m$. The variation of the width of the resonator concentrates the acoustic energy in the center of the device, away from the anchor points. Our simulation indicates that 70% of the dissipation in this curved structure is due to Akhiezer damping. The fourth mode (e) in Figure 5.4 is a length-extensional mode of a $600\mu m$ long, $20\mu m$ thick resonator, tethered to the substrate at its center point from Yang *et al.* [74]. Our simulation indicates that 54% of the energy loss is due to the Akhiezer effect. The last two modes (f) and (g) in Figure 5.4 are Lamé mode resonators where more than 50% of the measured energy loss is due to Akhiezer damping. These are the two black experimental points that lie above Woodruff's limit, as shown in Figure 4.2. The first Lamé mode (f) is a $400\mu m \times 400\mu m \times 20\mu m$ device fabricated and measured by Yang *et al.* [74] and

the second (g) is a $1000\mu\text{m} \times 1000\mu\text{m} \times 46\mu\text{m}$ reported by Wu *et al.* [54]. Despite the large size difference between these two devices, the measured fQ are quite similar. The simulated Akhiezer-limited fQ are identical due to the fact that both resonators are square and have the same strain profile where the shear strain dominates the deformation. Again the shear modes have a higher Akhiezer limited Q due to the reduction in the number of perturbed phonon modes that lead to dissipation. Shear mode resonators also have the highest measured fQ , indicating the need for an Akhiezer model that captures the dissipation limit. Without the new model presented in this work, it would appear as though these Lamé mode devices are already Akhiezer limited, attributing the deviations between devices to different material parameters, when in fact our model shows that the measured fQ is roughly half the Akhiezer limit, indicating that larger quality factors are attainable and that another damping mechanism (possibly anchor loss or TED) is contributing significantly to the loss in these resonators.

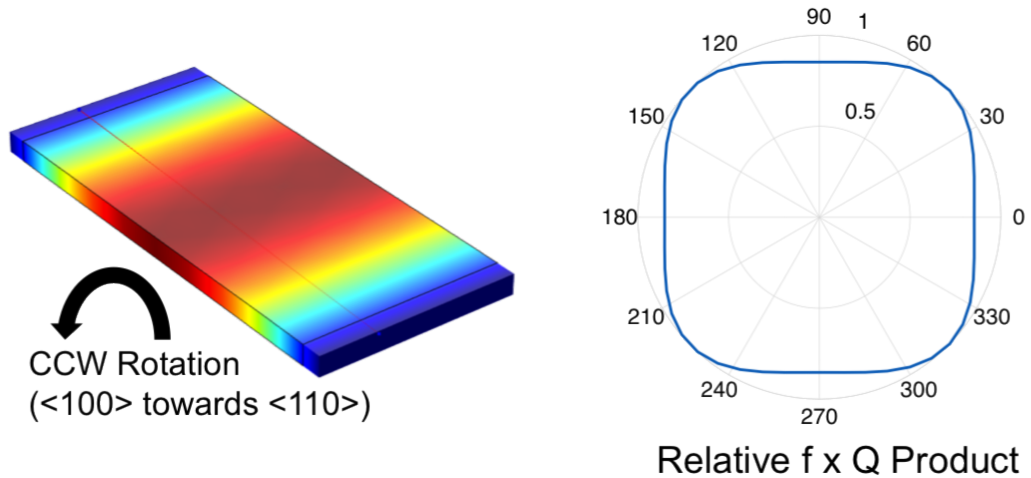


Figure 5.5: Mode-shape and simulated fQ product for a uniaxial extensional mode in single-crystal silicon as the device orientation is rotated counter-clockwise from the $[100]$ direction towards the $[110]$ direction. The simulation indicates an 17% increase in fQ for the $[110]$ orientation compared to the $[100]$ orientation.

Integration with Comsol[®] also allows us to analyze the effect of advanced device parameterization on the Akhiezer energy loss. Figure 5.5 shows the simulated fQ product for a uniaxial mode as the strain direction is rotated counter-clockwise from the [100] direction towards the [110] direction. The simulated results indicate a 17% increase in quality factor for the resonator oriented along the [110] axis. The simulation incorporates both anisotropic energy storage and energy loss. In general, resonators oriented along [110] directions tend to have higher simulated fQ products, which suggests that the Akhiezer damping contribution to the energy loss can be reduced by orienting the resonator along the primary flat of a [100] wafer.

Additionally, the integrated model can be used to simulate the temperature dependence of the Akhiezer loss. Figure 5.6 shows the temperature dependence of the Akhiezer loss for the same uniaxial extensional mode shown in Figure 5.5. Interestingly, the simulated result shows an increase in fQ as the temperature is increased from 77K to 300K. This may seem counter-intuitive given the fact that the expression in 4.3, at first glance, seems to indicate a $1/T$ dependence. However, when including the temperature dependence of all parameters including the SOEC that determine energy storage and resonant frequency, the TOEC which determine the energy loss, the specific heat, and the phonon lifetime derived from thermal conductivity measurements the temperature dependence flips. A least-squares fit estimates that $fQ \propto T^{0.58}$. The temperature dependence is largely due to the phonon lifetime which rapidly becomes longer when the temperature is reduced and is explained by noting that the parabolic frequency dependence in equation 4.3 indicates a resonance in the energy loss. The inset of Figure 5.6 plots Q as a function of the phonon lifetime τ . The minimum value (lowest Q) occurs when $\Omega\tau = 1$; any deviation from this condition leads to reduced energy loss and higher Q . As temperature is increased, the lifetime is reduced (moving from the blue circle at low-temperature to the red circle at high temperature) so the

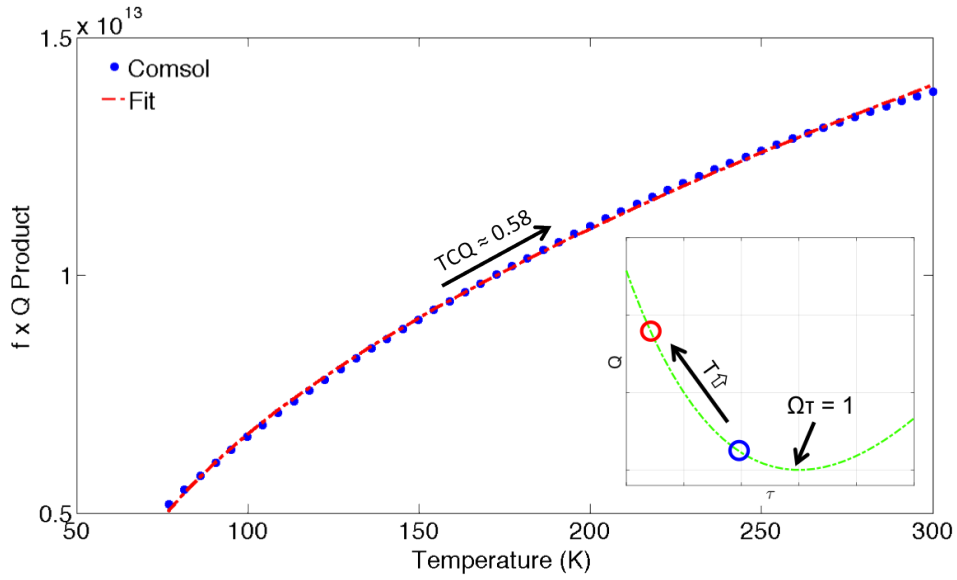


Figure 5.6: fQ product versus temperature from 77K to 300K for a uniaxial extensional mode in anisotropic single-crystal silicon. Despite the appearance that the quality factor expression in equation 4.3 is inversely proportional to temperature, inclusion of the temperature dependence of all relevant material parameters, most notably the phonon lifetime τ reveals a positive temperature coefficient of Q (TCQ) with a value of 0.58. The inset of Figure 5.6 plots Q as a function of the phonon lifetime τ . As temperature is increased, the lifetime is reduced, so that the resonator operating conditions move from the blue circle towards the red circle.

scattering rate ($1/\tau$) is increased and the mismatch between the scattering rate and the resonant frequency is larger, leading to reduced energy loss. Mechanical resonant frequencies are typically between 100kHz and 5GHz so the assumption that $\Omega\tau \ll 1$ is usually satisfied (with a cutoff frequency of 21GHz for silicon at room temperature). As we cool the resonator from room temperature to 77K, the scattering rate approaches the resonant frequency leading to more anharmonic phonon dissipation and reduced Q . If we cool the resonator further so that $\Omega\tau > 1$, the resonator is operating on the right side of the parabolic curve in the inset of

Figure 5.6 and the quality factor will begin to increase (as temperature is reduced). Thus, at temperatures approaching absolute zero, the Akhiezer model will predict zero dissipation and infinite Q , as we expect because at 0 K there are no thermal phonons that can scatter. There will be a minimum in the Q versus T curve when $\Omega\tau = 1$; for the resonator in Figure 5.6, this minima occurs at a temperature below which there is reliable data for all required material parameters. This minima is more readily observable at higher temperatures for resonators with higher resonant frequencies, so that the condition $\Omega\tau = 1$ occurs above 77K.

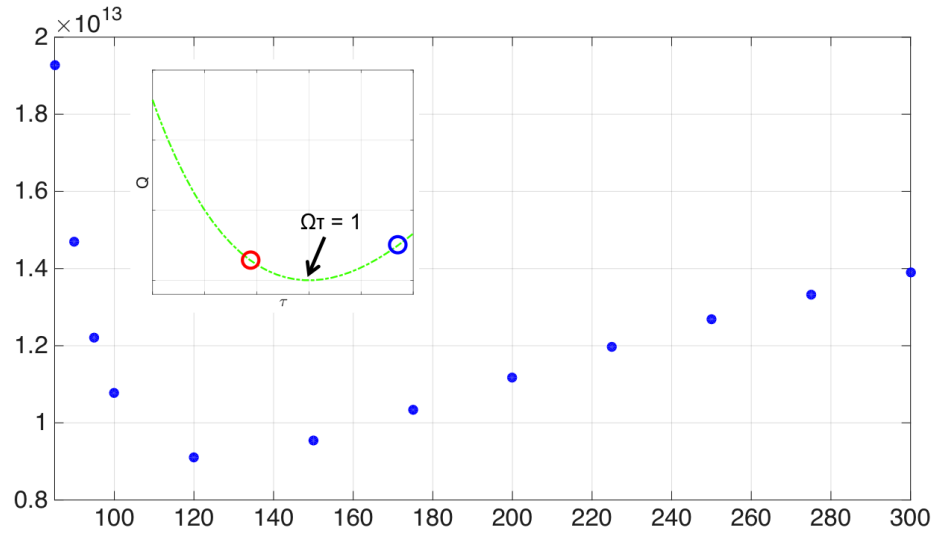


Figure 5.7: fQ product versus temperature from 77K to 300K for a high-frequency (1GHz) extensional mode in anisotropic single-crystal silicon. The inset of Figure 5.6 plots Q as a function of the phonon lifetime τ . As temperature is increased, the lifetime is reduced, so that the resonator operating conditions move from the blue circle towards the red circle. Our Akhiezer damping model predicts a minimum at 120K, and a rapidly increasing Q as the temperature is cooled below this value. We note, however, that the Akhiezer damping model presented in this work assumes that $\Omega\tau \ll 1$, so that interpretation of the results when $\Omega\tau > 1$ is not reliable.

This scenario is presented in Figure 5.7. At low temperature (blue circle in the inset of Figure 5.7) the resonator is operating to the right of the Q minima with τ . As the temperature increases the operating point crosses $\Omega\tau = 1$ moving the operating condition towards the red circle. Our Akhiezer damping model predicts a minimum at 120K, and a rapidly increasing Q as the temperature is cooled below this value. We note, however, that the Akhiezer damping model presented in this work assumes that $\Omega\tau \ll 1$, so that interpretation of the results when $\Omega\tau > 1$ is not reliable.

The integrated model also has the capability to simulate more complex modes. Figure 5.8 shows the temperature dependence of the Akhiezer dissipation for a $400\mu m \times 400\mu m \times 40\mu m$ square silicon resonator operating in different vibrational modes. The temperature dependencies are roughly similar, but we note that the overall Q can vary almost 4x for the same exact resonator. For applications where a specific mode-shape is not required, selecting different actuation electrodes and frequencies can potentially result in a higher quality factor. Others have noted that there may be variation in material parameters (specifically the mode-Grüneisen parameters) due to doping, for which there is no material data available [40]. We acknowledge that this variation may be present, and suggest that the temperature response of the quality factor be used as a robust way to verify the Akhiezer damping behavior of experimentally measured silicon resonators.

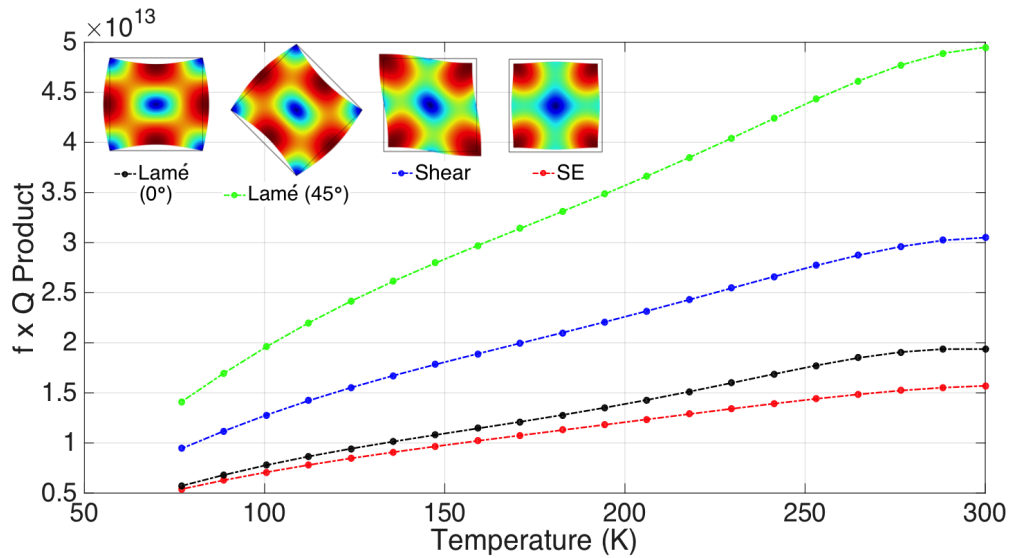


Figure 5.8: Simulated Akhiezer-limited fQ product versus temperature from 77K to 300K for different modes and orientations of a single-crystal silicon square resonator. Again a weak (less than linear) increase in fQ with temperature is predicted. The results indicate that the same resonator operated in different modes may have up to 4x improvement in Akhiezer-limited Q . For applications where a specific mode-shape is not required, selecting different actuation electrodes and frequencies can potentially result in a higher quality factor.

CHAPTER 6

Conclusion

This work details the derivation and evaluation of mechanical energy dissipation and the resulting quality factor in silicon nano and micromechanical resonators due to anharmonic phonon-phonon scattering (commonly referred to as Akhiezer damping). We provide a rigorous derivation of the anharmonic loss using the phonon Boltzmann transport equation and introduce the important simplifications that must be made in order to facilitate evaluation of the quality factor using known material parameters. The analytical result emphasizes that anharmonicity among phonon branches is quite fundamental to the Akhiezer effect and is required for energy loss to result. The anharmonicity is incorporated via inclusion of the mode-Grüneisen parameters, which are calculated as ratios of third-order to second-order elastic coefficients. Moreover, the expression for the quality factor derived in this work explicitly includes the anisotropic energy storage and loss in a cubic semiconductor or dielectric crystal by incorporating strain in all six strain directions in cubic crystals (rather than assuming uniaxial plane waves) and indicates that Akhiezer damping is not simply a material limit, but depends on the vibrational mode shape. The influence of the vibrational mode shape on the quality factor is presented for simple, first-order vibration modes in [100]-oriented silicon resonators assuming an infinite solid. The results show that shear or Lamé mode resonators have the highest quality factor limit, despite having lower energy storage moduli, meaning they are the best candidates for high-performance, Akhiezer-limited resonators. The reduced energy loss (and increased Q) for shear

modes is a consequence of the fact that the shear strain only perturbs the frequencies of 18 of the 39 normal phonon modes (as determined by calculating the mode-Grüneisen parameters for shear strain) in the diamond lattice, while normal strain perturbs the frequencies of all 39 phonon branches. Additionally, width-extensional vibration modes have a higher Akhiezer-limited quality factor than square-extensional modes (which, in turn, have a higher quality factor limit than cubic-extensional modes); this can be understood intuitively by noting that the square-extensional mode ‘resists’ the natural Poisson contraction of the solid, resulting in a larger phonon frequency perturbation.

The mode-dependence of the analytical result indicates the need to include the strain profile of the resonator in the Akhiezer damping model. Modern nano and micromechanical resonators are often operated in higher-order vibrational modes or have complex, 3-D geometries where the simplified formulations assuming an infinite solid do not provide a good estimate for the actual mode shape. These mode shapes are difficult, if not impossible, to solve for analytically. Thus, we extend the analytical result into the finite element domain via integration with a commercial finite element solver (Comsol Multiphysics[®]) in order to accurately predict the Akhiezer damping limit for modern MEMS devices. The finite element evaluation of the Akhiezer damping limit indicates that several silicon devices published in the literature have losses that are dominated (with up to 92% of the loss due to the Akhiezer effect) by anharmonic phonon scattering and are very close to the intrinsic quality factor limit. Integration with the finite element solver not only allows for meaningful comparisons between theory and experimental results, but also enables us to study the effect parametrization of device designs or operating conditions will have on the Akhiezer dissipation. Here, we include simulated results for orientation dependence as the device is rotated from the [100] toward the [110] direction, as well as the temperature dependence (including the temperature variation of all parameters) from 77K to 300K, which we suggest provides a ro-

bust method of verifying Akhiezer damping behavior in experimentally measured resonators.

Appendix A

Zener Model for Anelastic Relaxation in Solids

Zener's model for anelastic relaxations in solids is a generalization of Hooke's law that allows for the inclusion of mechanical relaxations that lead to energy dissipation. The formulation simply introduces a rate dependence in the stress-strain relation [41]. Instead of the typical elastic relation $\sigma = E\epsilon$, where σ is the stress, E is the Young's modulus and ϵ is the strain, Zener's model is formulated as follows

$$\sigma + \tau_\epsilon \frac{d\sigma}{dt} = E_R \epsilon + \tau_\sigma \frac{d\epsilon}{dt} \quad (\text{A.1})$$

where τ_ϵ and τ_σ are the characteristic time constants associated with adiabatically applied strain and stress, respectively. Essentially, this is a first-order formulation that introduces a lag between stress and strain. We note that at very low strain rates, the time derivatives in Zener's model can be ignored and the equation reduces to Hooke's law; hence, the relaxed Young's modulus describes the response of the solid under static conditions. When the stress and strain are time-harmonic, i.e. $\sigma = \sigma_0 e^{-i\Omega t}$ and $\epsilon = \epsilon_0 e^{-i\Omega t}$, the effective Young's modulus will be different in the low, intermediate and high frequency ranges, respectively. At sufficiently low frequencies where $\Omega \ll 1/\tau_\epsilon, 1/\tau_\sigma$, the expression reduces to Hooke's law with the real elastic modulus that is equal to the unrelaxed modulus associated with static deformations. At high frequencies, where $\Omega \gg 1/\tau_\epsilon, 1/\tau_\sigma$ the effective Young's modulus is again real-valued but takes on a different value, $E_U = \frac{\tau_\sigma}{\tau_\epsilon} E_R$, which we call the unrelaxed Young's modulus. The most interesting result occurs at intermediate frequencies, where the effective Young's modulus takes on the

complex-valued form

$$E(\Omega) = E_R \left(\frac{1 + \Omega^2 \tau^2}{1 + \Omega^2 \tau_\epsilon^2} - \frac{i\Omega\tau}{1 + \Omega^2 \tau_\epsilon^2} \Delta \right) = E_{eff} \left(1 - \frac{i\Omega\tau}{1 + \Omega^2 \tau^2} \Delta \right) \quad (\text{A.2})$$

where we have introduced the average relaxation time $\tau = \sqrt{\tau_\epsilon \tau_\sigma}$, the effective Young's modulus $E_{eff} = \frac{1 + \Omega^2 \tau^2}{1 + \Omega^2 \tau_\epsilon^2} E_R$ and the fractional difference modulus $\Delta = \frac{E_U - E_R}{E_R}$. The Young's modulus in equation A.2 is complex, so there will be a component of the stress that is out of phase with the strain. Returning to the time-harmonic formulation of the strain, where $\epsilon(t) = \epsilon_0 e^{-i\Omega t}$, the expression in equation A.2 can be used to determine the stress as

$$\sigma(t) = E_{eff} \left(1 - \frac{i\Omega\tau}{1 + \Omega^2 \tau^2} \right) \epsilon(t) \quad (\text{A.3})$$

The energy loss will be determined by the imaginary component of the stress. We can evaluate energy loss per cycle as real component of the work done by the stress, time-averaged over one period of oscillation

$$U_{loss/cycle} = - \left\langle \text{Re} \left[\sigma(t) \frac{d\epsilon(t)}{dt} \right] \right\rangle = \left\langle \frac{\Omega^2 \tau}{1 + \Omega^2 \tau^2} \Delta E_{eff} \epsilon^2(t) \right\rangle \quad (\text{A.4})$$

$$U_{loss/cycle} = \pi \frac{\Omega\tau}{1 + \Omega^2 \tau^2} \Delta E_{eff} \epsilon_0^2 \quad (\text{A.5})$$

Thus, the quality factor (see equation 1.1) is determined as,

$$Q = \frac{1 + \Omega^2 \tau^2}{\Omega\tau} \Delta \quad (\text{A.6})$$

Since Δ is the ratio of the difference between the unrelaxed and relaxed Young's moduli to the relaxed Young's modulus, we can consider it as a ratio between an effective loss modulus, which is determined by the physical phenomena that is characterized by the relaxation time τ , and an effective storage modulus. We see that both the Akhiezer and thermoelastic quality factors follow this formulation identically (see the Akhiezer formulation in equation 4.3 and the TED formulation

shown in figure 1.6), despite the fact that the physics behind the two dissipation mechanisms is fundamentally different.

This result should not be surprising, given that both the Akhiezer and thermoelastic damping are formulated based on a lag between the applied strain and the relaxation of the internal energy of the solid. In fact, we would expect any intrinsic damping mechanism to produce a quality factor expression that matches the form in equation A.6. The most notable feature of the Zener model is the minima in Q when $\Omega = 1/\tau$. This resonance is typically observed in one of two ways. The first is as a Q minima as the drive frequency, i.e. the mechanical resonant frequency, at a given temperature is varied and the lifetime τ remains constant, as we see with the Akhiezer loss in figure 4.2 . The second is as a resonance with temperature, where the drive frequency is kept relatively constant and the lifetime varies with the ambient temperature, as is observed in figure 5.7.

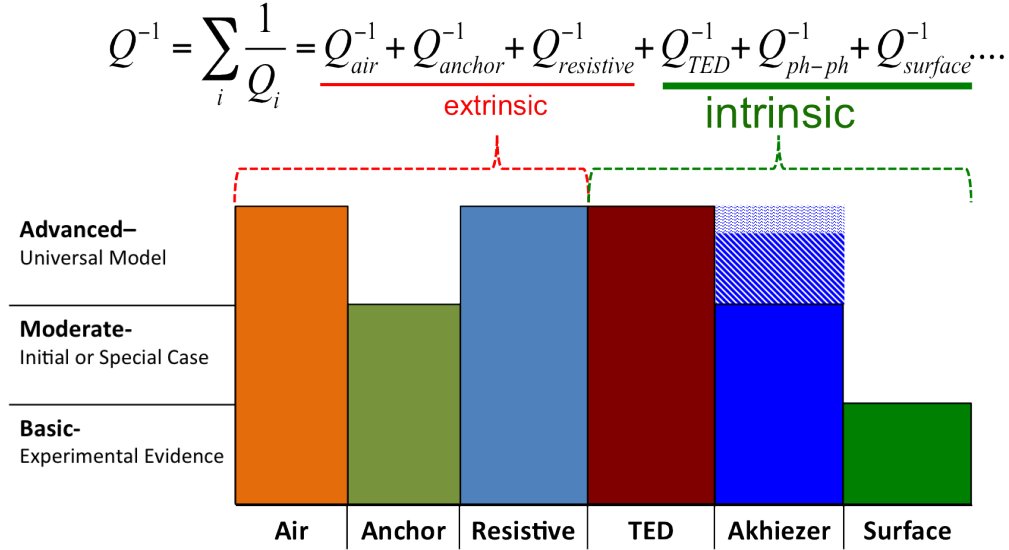
Appendix B

Surface Dissipation

Scaling of nano and micromechanical resonators to smaller sizes can lead to improved performance and enable new applications of these devices. While resonant frequency scales favorably with reduction in area [75] and is generally well-understood and modeled using finite-element techniques, the scaling of energy dissipation in these structures is not fully understood. The main body of the text details the derivation and evaluation of the bulk phonon-phonon dissipation that includes orientation- and mode-dependence and is integrated with finite element software to provide a universal model for Akhiezer damping. However, as noted in Chapter 1, one of the biggest barriers to a truly universal theory of dissipation is the fact that a number of damping mechanisms may contribute to the energy loss.

Surface dissipation is one such loss mechanism that has been observed experimentally, but does not have a sophisticated analytical model that can accurately describe the performance of mechanical resonators as they are scaled to sub-micron thicknesses. Figure B.1 shows the level of understanding of a number of dissipation mechanisms that may influence the quality factor of silicon resonators. The main contribution of this work is to fill the gap in the understanding of phonon dissipation and provide a universal model for Akhiezer damping, which is a bulk phenomenon. It is critically important to fully understand the bulk loss mechanisms (and their limits) before embarking on the challenging task of formulating an entirely new model that incorporates surface effects. Nevertheless, it is ev-

ident that bulk theories and simple extensions of these theories do not capture experimentally observed scaling of quality factor in nanomechanical resonators.



8

Figure B.1: Level of understanding of various dissipation mechanisms in silicon resonators. The main body of the text details a universal model for Akhiezer damping that provides a bulk limit on the quality factor of micromechanical due to phonon scattering, filling the gap in understanding. However, as devices are scaled to smaller sizes, bulk theories are no longer sufficient and new formulations that include the effects of finite sized resonators need to be developed.

Figure B.2 shows the quality factor of a number of silicon devices in the literature as a function of their volume. The survey, which includes devices measured at room temperature and cryogenic temperatures, shows a clear size-dependence of the quality factor in nano/micromechanical resonators. As device volume is reduced, the surface area to volume ratio increases, suggesting that surface effects will have a larger contribution to the energy loss. Despite a wealth of cases reporting surface-dependent Q , there is no predictive theory or convincing physical mechanism to explain the surface-mediated loss.

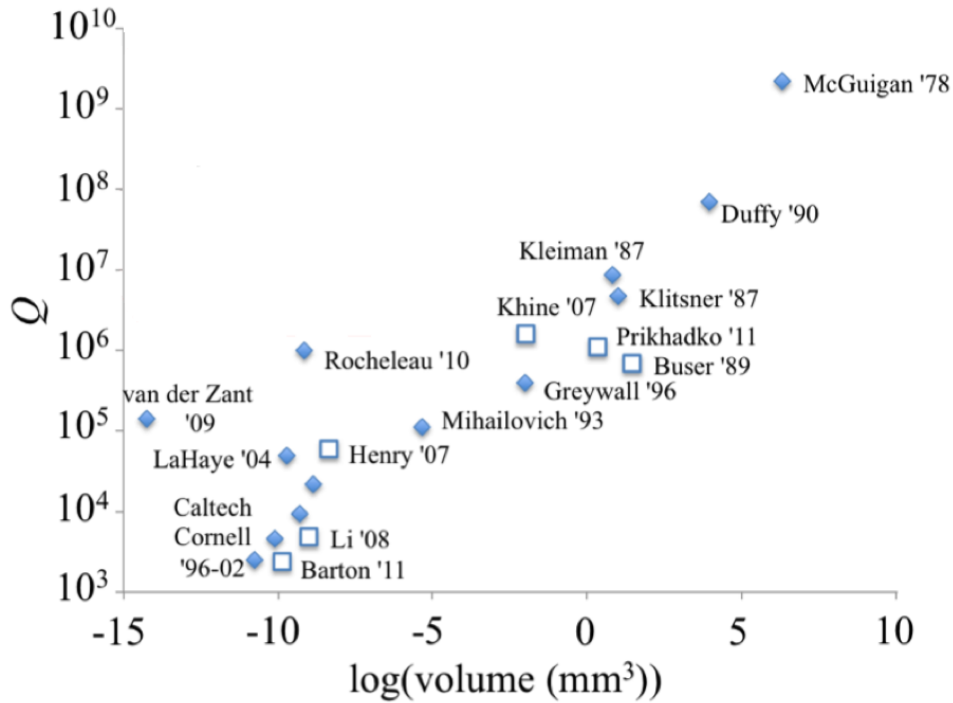


Figure B.2: A survey of published devices reveals a trend of decreasing Q with decreasing resonator size. This trend could be reversed with improved understanding of surface dissipation. Solid diamonds represent experiments performed at low temperature (<20 K), while hollow squares represent room temperature data.

The devices in figure B.2 represent a number of different resonator geometries and mode shapes that have been measured under different ambient conditions, so quantitative conclusions drawn from this survey are not necessarily reliable. Instead, a study of a single device type as the device dimensions are scaled can verify this trend of reduced Q as surface area to volume ratio increases. Here, we propose a device design and fabrication process to investigate this trend quantitatively.

In order to properly investigate surface dissipation, it is critical that the resonators used in this study be limited by surface effects, rather than other known loss mechanisms. We choose single-crystal silicon as the material system in order to avoid any grain-boundary effects that may be present in polycrystalline ma-

materials. We also select the torsional vibrational mode designed to have resonant frequencies between 1 and 20 MHz, in order to dramatically reduce the thermoelastic effect. The device design and finite element simulation of the torsional mode are given in figure B.3. The stiffness of this structure is governed largely by the dimensions of the two torsional beams, while variations in the size the large, central proof mass allow for control of the resonant frequency. Finally, the resonator must be sufficiently thin to ensure that the surface effects, rather than the bulk effects, dominate the performance of the device.

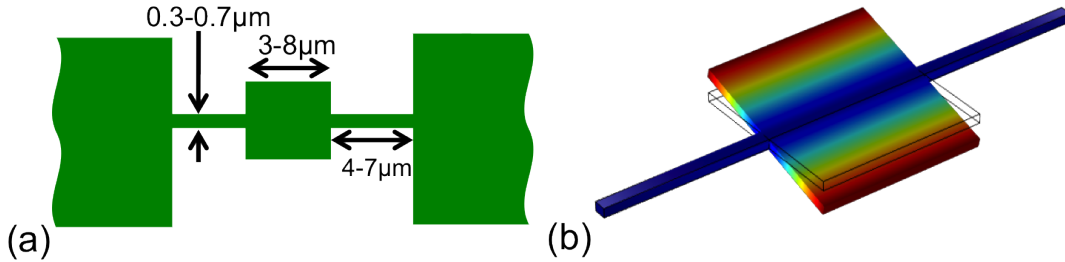


Figure B.3: Single-crystal silicon resonator showing (a) variations of device dimensions and (b) the torsional mode shape. Torsional modes are designed to be between 1 and 20 MHz.

A single mask process was used to fabricate sub-micron thick, single-crystal silicon resonators. The fabrication process is outlined in figure B.4. A silicon-on-insulator wafer with a device layer thickness of $2.5\mu\text{m}$ and a 400nm thick buried oxide is used as the source material. The device layer is thinned to less than 500nm via successive thermal oxidation and HF etching steps. The final thermal oxide is not stripped away in order to serve as a hard mask for subsequent etching to define the resonator. Finally, the device is released using HF vapor etching to remove the oxide hard mask and undercut the silicon so that the torsional paddle is a free-standing structure.

The energy dissipation in these resonators can be studied by measuring the frequency response of the resonator. Instead of using electrostatic actuation and

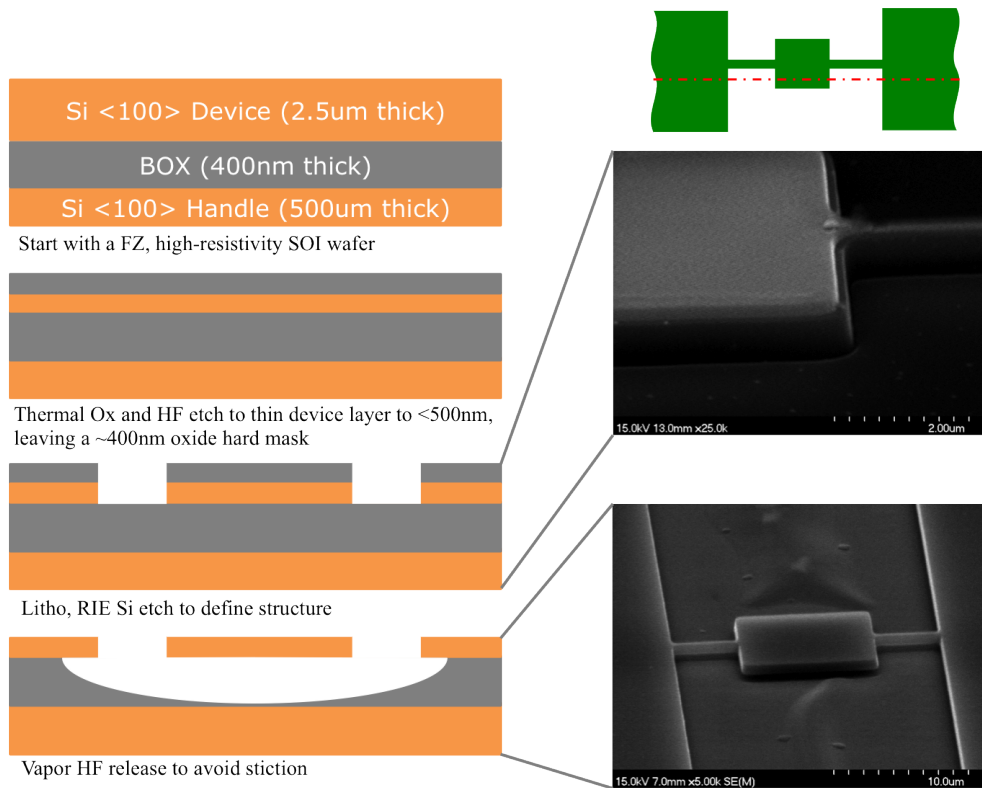


Figure B.4: Fabrication flow and scanning electron micrographs for sub-micron thick single-crystal silicon resonators. A series of thermal oxidation and HF etching steps are used to thin the device layer of a silicon-on-insulator wafer to a final thickness of less than 500 nm. A 400 nm thick thermal oxide remains and is used as a hard mask for the silicon etch that defines the resonator. Finally, the device is released via vapor HF etching to avoid stiction.

sensing, as is typical for nano and micromechanical silicon resonators, we use mechanical actuation and optical detection in order to avoid metal deposition that can introduce contaminants and other defects that can obscure trends in the intrinsic energy dissipation. A schematic of the experimental setup is shown in figure B.5 and a photograph of the actual laboratory setup is given in fig B.6. The resonator is operated in a vacuum chamber pumped down to a pressure below 10^{-4} mbar to eliminate air damping effects. The device is mounted on top of a transverse piezoelectric actuator that shakes the entire die, and the motion

is detected using differential laser Doppler vibrometry with a 633nm HeNe laser. This type of actuation will excite all vibrational modes; however, the resonator quality factor and modal separation are large enough to allow for simple identification of particular modes using resonant frequency. The vacuum cryostat is equipped with a temperature sensor, heater and continuous liquid nitrogen flow to vary the temperature between 77K and 400K.

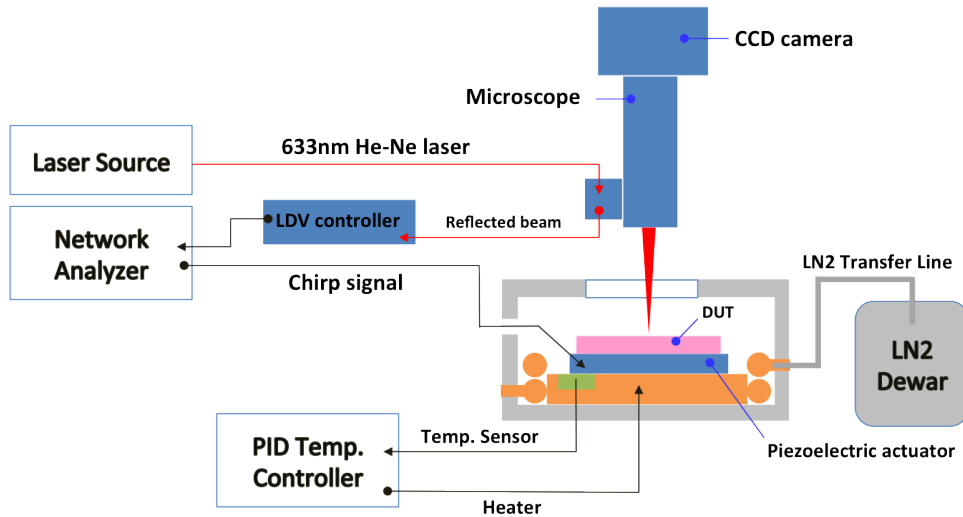


Figure B.5: Schematic of the experimental setup used to measure the frequency response of single-crystal resonators. The resonator is mounted in the vacuum cryostat on top of a piezoelectric actuator that mechanically shakes the entire die. Motion is sensed via differential laser doppler vibrometry. A heater and temperature sensor along with continuous liquid nitrogen flow and a proportional-integral-derivative controller are used to vary the temperature between 77K and 400K.

Figure B.7 shows the quality factor as temperature is varied for sub-micron thick silicon resonators. The blue and red points show the results for [100] and [111] oriented resonators fabricated and measured in this work along with two similar device responses from the literature [76, 77]. All of the sub-micron thick resonators show an increase in Q as temperature is increased around room

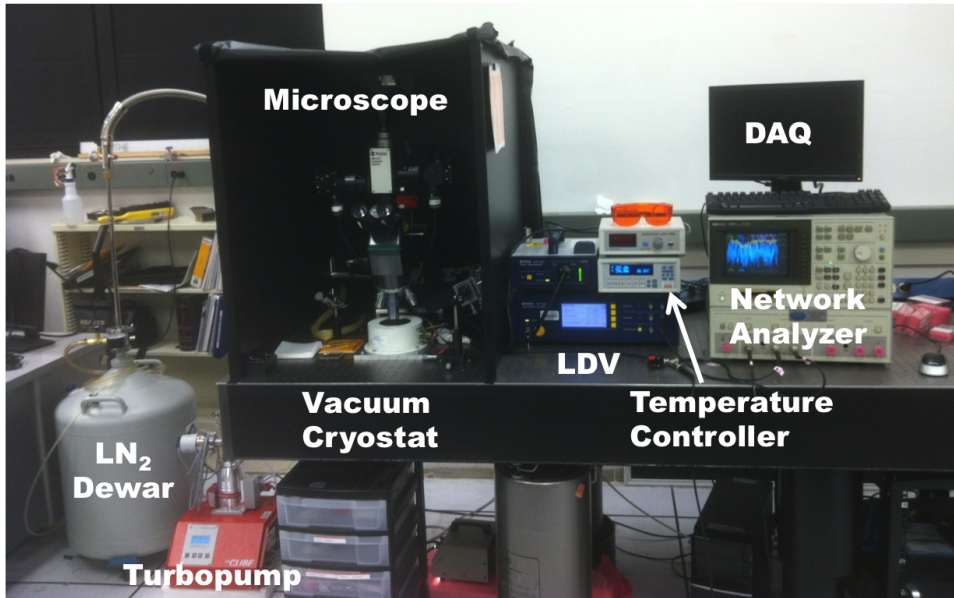


Figure B.6: Photograph of the experimental setup outlined in figure B.5.

temperature. Many also show the characteristic Debye minimum, which may be indicative of a relaxation process with a lifetime that is equal to $1/2\pi f$ at the temperature corresponding to the Q minima. We note that the resonant frequency variation (hollow blue circles) follows the expected shift due to temperature dependence of the Young's modulus.

Recent evidence has also shown that single monolayers can change the quality factor of single crystal silicon resonators. Figure B.8, from Richter and Hines [78], shows that different hydrocarbon based monolayers can alter the dissipation in single-crystal silicon resonators up to five times. Interestingly, the variation appears to be agnostic to monolayer chain length. The ethyl, dodecyl and octadecyl coatings have roughly the same quality factor. These three coatings share the same functional head group, but vary in chain length. This result suggests that the electronic surface structure, which determines the bonding at the surface, plays a major role in the resulting dissipation. Instead of using different monolayers to alter the dissipation, we propose electronic modulation of the surface

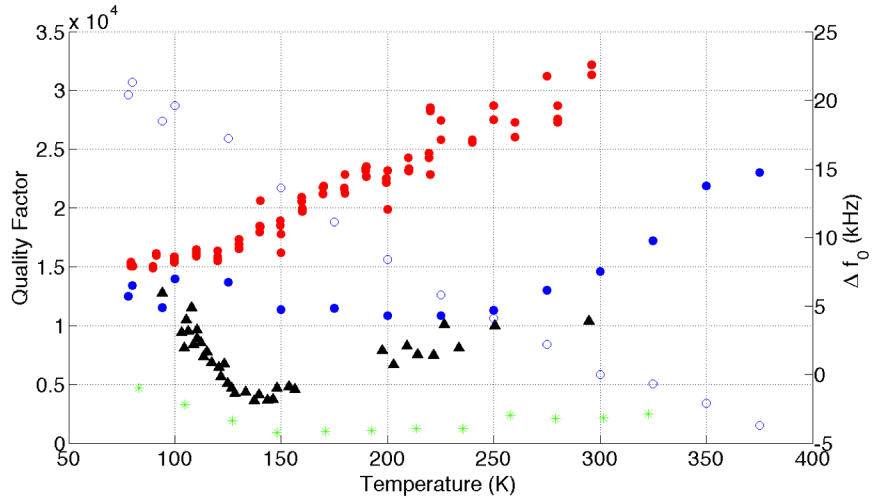


Figure B.7: Quality factor as a function of temperature from 77K to 400K for [100] (solid blue) and [111] (solid red) oriented resonators fabricated in this work along with results from two other sub-micron thick single-crystal silicon resonators from the literature [76, 77]. All of these thin devices show a trend of increasing Q as a function of temperature around room temperature. The characteristic Debye minima may be indicative of a relaxation process. The resonant frequency variation (hollow blue circles) for the [100] oriented resonator follows the expected shift due to temperature dependence of the Young’s modulus.

structure using an integrated P-I-N resonator. This allows for in situ modulation of the surface charge so that the theory of mobile carrier influence on mechanical energy dissipation can be assessed directly. The proposed fabrication flow is given in figure B.9.

The P-I-N structure allows for dynamic depletion and accumulation of mobile charge carriers on the surface. The 2-D electronic device simulation in figure B.10, shows that the carrier concentration can be varied by nine orders of magnitude using both reverse and forward biased P-I-N diodes. Carriers may also be injected via illumination of the resonator with light with a photon energy above the bandgap of silicon.

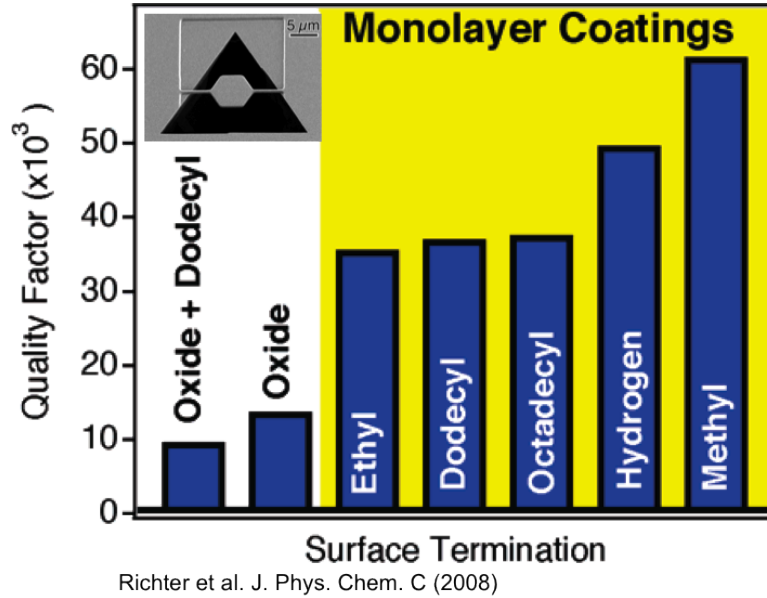


Figure B.8: Quality factor for sub-micron thick single-crystal torsional resonators fabricated on [111] substrates with different monolayer coatings. These results (from [78]) show that the quality factor can vary up to five times by varying the monolayer coating. Interestingly, the ethyl, dodecyl and octadecyl coatings have roughly the same dissipation, suggesting that electronic surface structure plays a key role in the surface dissipation mechanism.

In this appendix we have motivated the need for further investigation of energy dissipation mechanisms in sub-micron thick resonators where general trends in resonator Q suggest that surface-mediated energy loss plays an important role. We use torsional, single-crystal silicon resonators as a test bed for investigation of surface phenomena due to their insensitivity to grain-boundary scattering and thermoelastic dissipation. We include fabrication details and initial quality factor vs temperature results for intrinsic single-crystal devices showing an increase in Q with increasing temperature near 296K. Finally, we propose an integrated P-I-N resonator in order to assess the effect of surface charge modulation via depletion and accumulation of the resonator without altering the mass or operating conditions of the resonator.

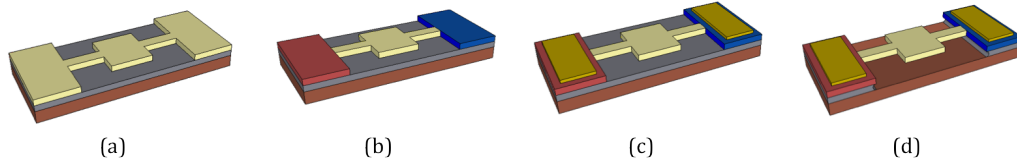


Figure B.9: Fabrication flow for single crystal integrated P-I-N resonators on an silicon-on-insulator substrate. (a) Pattern and etch resonator layer from lightly doped p-type (yellow) silicon-on-insulator (SOI) wafer. (b) Pattern and implant P+ region (red) followed by N+ region (blue), ensuring surface doping via double implantation. (c) Pattern and etch metal contacts (gold). (d) HF vapor etch to undercut oxide and release.

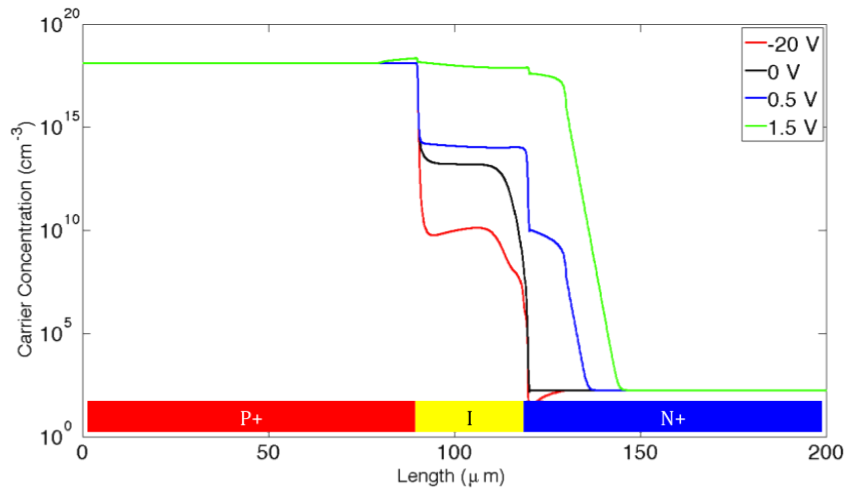


Figure B.10: 2-D device simulation of a P-I-N integrated resonator depletion and accumulation under different biases using Taurus Medici. Carrier concentration can be controlled over nine orders of magnitude with reverse (-20V) and forward bias (+1.5V). The entire resonator (beams and paddle) is contained within the intrinsic region.

REFERENCES

- [1] JC Eloy, M Potin, E Mounier, and P Roussel. Advanced microsystems for automotive applications 2006. In *International Forum on Advanced Microsystems for Automotive Applications (AMAA)*. ISBN, pages 3–540, 2005.
- [2] R. Neul, U. M. Gomez, K. Kehr, W. Bauer, J. Classen, C. Doring, E. Esch, S. Gotz, J. Hauer, B. Kuhlmann, C. Lang, M. Veith, and R. Willig. Micro-machined angular rate sensors for automotive applications. *IEEE Sensors Journal*, 7(2):302–309, Feb 2007.
- [3] Aaron Partridge, Markus Lutz, Bongsang Kim, Matthew Hopcroft, Rob N Candler, Thomas W Kenny, Kurt Petersen, and Masayoshi Esashi. Mems resonators: getting the packaging right. In *Proceedings of the 9th SEMI Microsystem/MEMS Seminar (SEMICON), Makuhari, Japan*, pages 55–58, 2005.
- [4] L. Lin, C. T. C. Nguyen, R. T. Howe, and A. P. Pisano. Microelectromechanical filters for signal processing. In *Micro Electro Mechanical Systems, 1992, MEMS '92, Proceedings. An Investigation of Micro Structures, Sensors, Actuators, Machines and Robot. IEEE*, pages 226–231, Feb 1992.
- [5] C. T. C. Nguyen, L. P. B. Katehi, and G. M. Rebeiz. Micromachined devices for wireless communications. *Proceedings of the IEEE*, 86(8):1756–1768, Aug 1998.
- [6] R. Ruby, P. Bradley, D. Clark, D. Feld, T. Jamneala, and Kun Wang. Acoustic fbar for filters, duplexers and front end modules. In *Microwave Symposium Digest, 2004 IEEE MTT-S International*, volume 2, pages 931–934 Vol.2, June 2004.
- [7] H. Chandralalim, D. Weinstein, Lih Feng Cheow, and S. A. Bhave. Channel-select micromechanical filters using high-k dielectrically transduced mems resonators. In *19th IEEE International Conference on Micro Electro Mechanical Systems*, pages 894–897, 2006.
- [8] D. Weinstein and S. A. Bhave. Internal dielectric transduction in bulk-mode resonators. *Journal of Microelectromechanical Systems*, 18(6):1401–1408, Dec 2009.
- [9] G. Piazza, P. J. Stephanou, and A. P. Pisano. Single-chip multiple-frequency aln mems filters based on contour-mode piezoelectric resonators. *Journal of Microelectromechanical Systems*, 16(2):319–328, April 2007.
- [10] M. Rais-Zadeh and F. Ayazi. Small-bandwidth integrated tunable bandpass filters for gsm applications. In *Micro Electro Mechanical Systems, 2008*.

- MEMS 2008. IEEE 21st International Conference on*, pages 1032–1035, Jan 2008.
- [11] F. Ayazi. Mems for integrated timing and spectral processing. In *2009 IEEE Custom Integrated Circuits Conference*, pages 65–72, Sept 2009.
- [12] Philip S Waggoner and Harold G Craighead. Micro-and nanomechanical sensors for environmental, chemical, and biological detection. *Lab on a Chip*, 7(10):1238–1255, 2007.
- [13] Thomas P. Burg, Michel Godin, Scott M. Knudsen, Wenjiang Shen, Greg Carlson, John S. Foster, Ken Babcock, and Scott R. Manalis. Weighing of biomolecules, single cells and single nanoparticles in fluid. *Nature*, 446(7139):1066–1069, 04 2007.
- [14] H. Zhang, M. S. Marma, S. K. Bahl, E. S. Kim, and C. E. McKenna. Sequence specific label-free dna sensing using film-bulk-acoustic-resonators. *IEEE Sensors Journal*, 7(12):1587–1588, Dec 2007.
- [15] A. Lin, Hongyu Yu, M. S. Waters, Eun Sok Kim, and S. D. Goodman. Explosive trace detection with fbar-based sensor. In *Micro Electro Mechanical Systems, 2008. MEMS 2008. IEEE 21st International Conference on*, pages 208–211, Jan 2008.
- [16] H. J. Lee, K. K. Park, O. Oralkan, M. Kupnik, and B. T. Khuri-Yakub. Cmut as a chemical sensor for dmmp detection. In *2008 IEEE International Frequency Control Symposium*, pages 434–439, May 2008.
- [17] H. Wohltjen, A. W. Snow, W. R. Barger, and D. S. Ballantine. Trace chemical vapor detection using saw delay line oscillators. *IEEE Transactions on Ultrasonics, Ferroelectrics, and Frequency Control*, 34(2):172–178, March 1987.
- [18] Y. T. Yang, C. Callegari, X. L. Feng, § K. L. Ekinici, , and M. L. Roukes*. Zeptogram-scale nanomechanical mass sensing. *Nano Letters*, 6(4):583–586, 2006. PMID: 16608248.
- [19] KL Ekinici, XMH Huang, and ML Roukes. Ultrasensitive nanoelectromechanical mass detection. *Applied Physics Letters*, 84(22):4469–4471, 2004.
- [20] D. Rugar, R. Budakian, H. J. Mamin, and B. W. Chui. Single spin detection by magnetic resonance force microscopy. *Nature*, 430(6997):329–332, 07 2004.
- [21] A. D. Oâ™Connell, M. Hofheinz, M. Ansmann, Radoslaw C. Bialczak, M. Lenander, Erik Lucero, M. Neeley, D. Sank, H. Wang, M. Weides, J. Wenner, John M. Martinis, and A. N. Cleland. Quantum ground state and single-phonon control of a mechanical resonator. *Nature*, 464(7289):697–703, 04 2010.

- [22] T. Rocheleau, T. Ndukum, C. Macklin, J. B. Hertzberg, A. A. Clerk, and K. C. Schwab. Preparation and detection of a mechanical resonator near the ground state of motion. *Nature*, 463(7277):72–75, 01 2010.
- [23] V. B. Braginsky, V. P. Mitrofanov, V. I. Panov, and C. Eller. *Systems with small dissipation*. University of Chicago Press, 1985.
- [24] Xu Wang, Wenqi Wu, Bing Luo, Zhen Fang, Yun Li, and Qingan Jiang. Force to rebalance control of hrg and suppression of its errors on the basis of fpga. *Sensors*, 11(12):11761–11773, 2011.
- [25] D. B. Leeson. A simple model of feedback oscillator noise spectrum. *Proceedings of the IEEE*, 54(2):329–330, Feb 1966.
- [26] Y. Hwang, F. Gao, A. J. Hong, and R. N. Candler. Porous silicon resonators for improved vapor detection. *Journal of Microelectromechanical Systems*, 21(1):235–242, Feb 2012.
- [27] Clarence Zener. Internal friction in solids. i. theory of internal friction in reeds. *Physical Review*, 52(3):230–235, 1937.
- [28] Clarence Zener. Internal friction in solids ii. general theory of thermoelastic internal friction. *Physical Review*, 53(1):90–99, 1938.
- [29] A. Duwel, R. N. Candler, T. W. Kenny, and M. Varghese. Engineering mems resonators with low thermoelastic damping. *Journal of Microelectromechanical Systems*, 15(6):1437–1445, Dec 2006.
- [30] R. N. Candler, A. Duwel, M. Varghese, S. A. Chandorkar, M. Hopcroft, W.-T. Park, B. Kim, G. Yama, A. Partridge, M. Lutz, and T. W. Kenny. Impact of geometry on thermoelastic dissipation in micromechanical resonant beams. *J. Microelectromech. S.*, 15(4):927–934, 2006.
- [31] S. A. Chandorkar, R. N. Candler, A. Duwel, R. Melamud, M. Agarwal, K. E. Goodson, and T. W. Kenny. Multimode thermoelastic dissipation. *J. Appl. Phys.*, 105(4):043505, 2009.
- [32] HUMPHREY J Maris. Interaction of sound waves with thermal phonons in dielectric crystals. *Physical Acoustics*, 8:279–345, 1970.
- [33] A. Akhiezer. On the absorption of sound in solids. *J. Phys. USSR*, 1:277, 1939.
- [34] W. P. Mason and T. B. Bateman. Ultrasonic-wave propagation in pure silicon and germanium. *J. Acoust. Soc. Am.*, 36(4):644–652, 1964.
- [35] R. Nava, M. P. Vecchi, J. Romero, and B. Fernandez. Akhiezer damping and the thermal conductivity of pure and impure dielectrics. *Phys. Rev. B*, 14(2):800, 1976.

- [36] A. A. Kiselev and G. J. Iafrate. Phonon dynamics and phonon assisted losses in euler-bernoulli nanobeams. *Phys. Rev. B*, 77:205436, May 2008.
- [37] C. Kittel. *Introduction to solid state physics*. Wiley, 2005.
- [38] W.P. Mason. *Physical Acoustics: Principles and Methods*, volume IIIB. Academic Press Inc., 1965.
- [39] T. O. Woodruff and H. Ehrenreich. Absorption of sound in insulators. *Phys. Rev.*, 123(5):1553, 1961.
- [40] S. Ghaffari, S. A. Chandorkar, S. Wang, E. J. Ng, C. H. Ahn, V. Hong, Y. Yang, and T. W. Kenny. Quantum limit of quality factor in silicon micro and nano mechanical resonators. *Sci. Rep.*, 3:3244 EP –, 11 2013.
- [41] A. N. Cleland. *Foundations of nanomechanics: from solid-state theory to device applications*. Springer Science & Business Media, 2013.
- [42] H. H. Barrett and M. G. Holland. Critique of current theories of akhieser damping in solids. *Phys. Rev. B*, 1(6):2538, 1970.
- [43] G. G. Sahasrabudhe and S. D. Lambade. Temperature dependence of the collective phonon relaxation time and acoustic damping in ge and si. *J. Phys. Chem. Solids*, 60(6):773–785, 1999.
- [44] L. G. Merkulov, R. V. Kovalenok, and E. V. Konovodehenko. Orientation dependence of the absorption of ultrasound in alkali halide crystals. *Fiz. Tverd. Tela+*, 11(10):2241, 1970.
- [45] S. D. Lambade, G. G. Sahasrabudhe, and S. Rajagopalan. Temperature dependence of acoustic attenuation in silicon. *Phys. Rev. B*, 51(22):15861, 1995.
- [46] A. Nowick and D. Berry. *Anelastic relaxation in crystalline solids*, acad. Press, New York, 1972.
- [47] H. E. Bömmel and K. Dransfeld. Excitation and attenuation of hypersonic waves in quartz. *Phys. Rev.*, 117(5):1245–1252, 1960.
- [48] K. Kunal and N. R. Aluru. Akhiezer damping in nanostructures. *Phys. Rev. B*, 84:245450, Dec 2011.
- [49] K. Brugger. Generalized grüneisen parameters in the anisotropic debye model. *Physical Review*, 137(6A):A1826–A1827, 1965.
- [50] M. Hopcroft, W. D. Nix, and T. W. Kenny. What is the young’s modulus of silicon? *J. Microelectromech. S.*, 19(2):229–238, 2010.

- [51] V. P. Mitrofanov, L. G. Ovodova, and V. S. Shiyan. Longitudinal sound-wave attenuation in sapphire due to phonon-phonon interaction. *Fiz. Tverd. Tela+*, 22(5):1545–1547, 1980.
- [52] Y. V. Ilisavskii and V. M. Sternin. Lattice absorption of high-frequency sound in silicon. *Sov. Phys. Sol. St.*, 27(2):236–239, 1985.
- [53] R. Tabrizian, M. Rais-Zadeh, and F. Ayazi. Effect of phonon interactions on limiting the f.q product of micromechanical resonators. In *Proc. IEEE Int. Conf. Solid State Sens., Actuator Microsyst.*, pages 2131–2134, June 2009.
- [54] G. Wu, D. Xu, B. Xiong, and Y. Wang. High single crystal silicon micromechanical resonators with hybrid etching process. *IEEE Sens. J.*, 12(7):2414–2415, 2012.
- [55] D. Weinstein and S. Bhave. Internal dielectric transduction in bulk-mode resonators. *J. Microelectromech. S.*, 18(6):1401–1408, 2009.
- [56] S.-S. Li, Y.-W. Lin, Y. Xie, Z. Ren, and C. T.-C. Nguyen. Micromechanical ”hollow-disk” ring resonators. In *Proc. IEEE Micr. Elect.*, pages 821–824, 2004.
- [57] M. Ziaei-Moayyed and R. T. Howe. Higher-order dielectrically transduced bulk-mode ring resonator with low motional resistance. In *Proc. IEEE Intl. Freq. Symp.*, pages 19–24, 2010.
- [58] L. Khine and M. Palaniapan. High-q bulk-mode soi square resonators with straight-beam anchors. *J. Micromech. and Microeng.*, 19(1):015017, 2009.
- [59] J. E.-Y. Lee and A. A. Seshia. 5.4-mhz single-crystal silicon wine glass mode disk resonator with quality factor of 2 million. *Sensor. and Actuat. A-Phys.*, 156(1):28–35, 2009.
- [60] S. Pourkamali, G. K. Ho, and F. Ayazi. Low-impedance vhf and uhf capacitive silicon bulk acoustic-wave resonators-part ii: Measurement and characterization. *IEEE T. Electr. Dev.*, 54(8):2024, 2007.
- [61] A. K. Samarao, G. Casinovi, and F. Ayazi. Passive tcf compensation in high q silicon micromechanical resonators. In *Proc. IEEE Micr. Elect.*, pages 116–119, 2010.
- [62] H. M. Lavasani, A. K. Samarao, G. Casinovi, and F. Ayazi. A 145mhz low phase-noise capacitive silicon micromechanical oscillator. In *Int. El. Devices Meet.*, pages 1–4, 2008.
- [63] J. E.-Y. Lee, B. Bahreyni, Y. Zhu, and A. Seshia. A single-crystal-silicon bulk-acoustic-mode microresonator oscillator. *Int. El. Devices Meet.*, 29(7):701–703, 2008.

- [64] C. Tu and J. E.-Y. Lee. Increased dissipation from distributed etch holes in a lateral breathing mode silicon micromechanical resonator. *Appl. Phys. Lett.*, 101(2):023504, 2012.
- [65] H. Zhu, Y. Xu, and J. E.-Y. Lee. Piezoresistive readout mechanically coupled lame; mode soi resonator with of a million. *J. Microelectromech. S.*, 24(4):771–780, Aug 2015.
- [66] J. Wang, Z. Ren, and C. T.-C. Nguyen. 1.156-ghz self-aligned vibrating micromechanical disk resonator. *IEEE T. Ultrason. Ferr.*, 51(12):1607–1628, 2004.
- [67] J. R. Clark, W.-T. Hsu, M. Abdelmoneum, and C. T.-C. Nguyen. High-q uhf micromechanical radial-contour mode disk resonators. *J. Microelectromech. S.*, 14(6):1298–1310, 2005.
- [68] L. Landau and G. Rumer. Absorption of sound in solids. *Phys. Z. Sowjetunion*, 11(18), 1937.
- [69] Y. S. Ju and K. E. Goodson. Phonon scattering in silicon films with thickness of order 100 nm. *Appl. Phys. Lett.*, 74(20):3005–3007, 1999.
- [70] F. Yang and C. Dames. Mean free path spectra as a tool to understand thermal conductivity in bulk and nanostructures. *Phys. Rev. B*, 87:035437, Jan 2013.
- [71] K. T. Regner, D. P. Sellan, Z. Su, C. H. Amon, A. J. H. McGaughey, and J. A. Malen. Broadband phonon mean free path contributions to thermal conductivity measured using frequency domain thermoreflectance. *Nat. Commun.*, 4:1640, 03 2013.
- [72] E.J. Ng, V.A. Hong, Yushi Yang, Chae Hyuck Ahn, C.L.M. Everhart, and T.W. Kenny. Temperature dependence of the elastic constants of doped silicon. *J. Microelectromech. S.*, 24(3):730–741, June 2015.
- [73] A. K. Samarao, G. Casinovi, and F. Ayazi. Passive tcf compensation in high q silicon micromechanical resonators. In *Micro Electro Mechanical Systems (MEMS), 2010 IEEE 23rd International Conference on*, pages 116–119, Jan 2010.
- [74] Y. Yang, E. J. Ng, Y. Chen, I. B. Flader, and T. W. Kenny. A unified epi-seal process for fabrication of high-stability microelectromechanical devices. *Journal of Microelectromechanical Systems*, 25(3):489–497, June 2016.
- [75] XMH Huang, XL Feng, CA Zorman, M Mehregany, and ML Roukes. Vhf, uhf and microwave frequency nanomechanical resonators. *New Journal of Physics*, 7(1):247, 2005.

- [76] Kevin Y Yasumura, Timothy D Stowe, Eugene M Chow, Timothy Pfafman, Thomas W Kenny, Barry C Stipe, and Daniel Rugar. Quality factors in micron-and submicron-thick cantilevers. *Journal of microelectromechanical systems*, 9(1):117–125, 2000.
- [77] A Olkhovets, S Evoy, DW Carr, JM Parpia, and HG Craighead. Actuation and internal friction of torsional nanomechanical silicon resonators. *Journal of Vacuum Science & Technology B*, 18(6):3549–3551, 2000.
- [78] Amy M Richter, Debodhonyaa Sengupta, and Melissa A Hines. Effect of surface chemistry on mechanical energy dissipation: Silicon oxidation does not inherently decrease the quality factor. *The Journal of Physical Chemistry C*, 112(5):1473–1478, 2008.